Constraining mantle density structure using geological evidence of surface uplift rates: The case of the African Superplume

Michael Gurnis

Seismological Laboratory, California Institute of Technology, Pasadena, California 91125
(gurnis@caltech.edu)

Jerry X. Mitrovica

Department of Physics, University of Toronto, Toronto, Canada (jxm@physics.utoronto.ca)

Jeroen Ritsema

Seismological Laboratory, California Institute of Technology, Pasadena, California 91125
(jeroen@gps.caltech.edu)

Hendrik-Jan van Heijst

Seismological Laboratory, California Institute of Technology, Pasadena, California 91125
(hendrik@gps.caltech.edu)

Now at Dedelstraat 9-II, 2596 RA Den Haag, Netherlands

[1] **Abstract:** We explore the hypothesis that southern Africa is actively being uplifted by a large-scale, positively buoyant structure within the mid-lower mantle. Using a new formulation in which dynamic topography and uplift rate are jointly used, we place constraints on mantle density and viscosity. The solution of the momentum equation is coupled with the advection of the density field to solve for the surface uplift rate in both an axisymmetric and fully spherical geometry. We demonstrate how dynamic topography and its rate of change depend on density and lateral and radial variations in viscosity. In the full spherical models the geometry of mantle density is derived by scaling a tomographic shear velocity model. Using a variety of geologic observations, we estimate residual topography (i.e., the topography remaining after shallow sources of density are removed) and an average Cenozoic uplift rate to be 300–600 m and 5–30 m/Myr, respectively, for southern Africa. We are able to satisfy these constraints with a mantle model in which the mid-lower mantle beneath southern Africa is 0.2% less dense and has a viscosity of $\sim10^{22}$ Pa s. In addition, if the continental lithosphere is thick beneath southern Africa, as suspected from seismic inversions, and has a high effective viscosity, then we find that southern Africa can be further elevated owing to increased coupling between the deep mantle and surface. We show that recent estimates of mantle density, suggesting that the lowest parts of the African anomaly may be anomalously dense are compatible with geologic constraints. We conclude that uplift rate, when combined with estimates of present-day dynamic topography, provides a powerful tool to constrain the properties of the deep mantle.

1. Introduction

[2] Significant seismic velocity variations have been resolved in the deep mantle, but the origin and nature of these anomalies remain controversial. It has long been recognized that seismic velocities are higher than average in the deep mantle below the circum-Pacific, while they are lower than average beneath Africa and the central Pacific [*Dziewonski*, 1984; *Dziewonski and Woodhouse*, 1987]. The high velocities are present below regions of long-term subduction, while the lower velocities are in regions that have been devoid of subduction for an extensive period of geologic time. The standard interpretation of this pattern, which is most evident at degree 2, is that seismic velocities are higher than average in regions that are cold, while seismic velocities are lower than average in regions that are hot. This view has gained support from recent tomographic inversions showing high seismic velocity structures down to the core mantle boundary that are attached to present-day subduction beneath Central America and Japan [*Grand et al.*, 1997; *van der Hilst et al.*, 1997; *van Heijst et al.*, 1999]. In general, high-velocity structures beneath circum-Pacific subduction zones are complex, but much of this complexity may be related to a combination of the time dependence of the subduction process, on the one hand, and partial resistance offered by both the phase transition at 660-km depth and radial variations in viscosity, on the other [*Zhong and Gurnis*, 1995].

[3] The most significant low seismic velocity structure in the deep mantle is located beneath southern Africa and the southern Atlantic Ocean [*Dziewonski and Woodhouse*, 1987; *Su et al.*, 1994; *Li and Romanowicz*, 1996; *Grand et al.*, 1997]. As the resolution of tomographic inversions has improved, the amplitude of the anomaly and its sharpness have increased. From an analysis of differential travel times of S, ScS, and SKS arrivals in eastern Africa, *Ritsema et al.* [1998] suggest that the low-velocity anomaly extends at least 1500 km from the core mantle boundary and has an average velocity that is 3% lower than normal mantle. Moreover, they suggest that the sides of the anomaly are rather sharp with shear velocity varying in amplitude by 2% over a ~300-km length scale. The long-standing interpretation of the African seismic anomaly is that it represents a long-lived, hot mantle upwelling [*Hager et al.*, 1985]. The long-wavelength lower than average seismic velocities generally correlate with long-wavelength geoid highs [e.g., *Hager et al.*, 1985] and these geoid highs contain most of the world's hotspots [*Chase*, 1979]. Southern Africa has a high topography [*Nyblade and Robinson*, 1994] as well as an unusual physiography and hypsometry indicative of uplift that may be dynamically supported by flow within the lower mantle [*Hager et al.*, 1985; *Lithgow-Bertelloni and Silver*, 1998]. This interpretation is qualitatively consistent with a range of observations that shows that Africa is experiencing active interplate volcanism and rifting [*Burke*, 1996].

[4] As support for the connection between deep-seated seismic anomalies and thermal signatures associated with large-scale mantle convection has grown, contradictory observations have emerged. Seismic tomographic inversions indicate that bulk sound speed and

shear wave speed are either poorly correlated or anticorrelated below 2000-km depth [*Bolton*, 1996; *Su and Dziewonski*, 1997; *Kennett et al.*, 1998; *Masters et al.*, 1999; *Ishii and Tromp*, 1999]. The ratio of bulk sound velocity to shear velocity may increase in the lower third of the mantle [*van der Hilst and Karason*, 1999]. These results suggest the presence of wide-spread chemical heterogeneity within the deep mantle. Results independent of body wave travel times have been obtained from normal modes in which compressional velocity, shear velocity, density, and boundary topography have been simultaneously inverted [*Ishii and Tromp*, 1999; *Kuo and Romanowicz*, 1999]. *Ishii and Tromp* [1999] obtain the unexpected result that both the Pacific and African anomalies are ≈1% denser than average in the region extending from the core mantle boundary to 500 km above it. From the canonical thermal model we would have expected the anomalies to be less dense everywhere. However, *Kuo and Romanowicz* [1999] obtain different results for mantle density and conclude that lateral density anomalies cannot be determined with present seismic data sets.

[5] In the model of *Lithgow-Bertelloni and Silver* [1998], southern Africa is dynamically supported by low-density structures that they infer from the low-shear velocity structure; however, the lower part of this structure has been estimated by *Ishii and Tromp* [1999] to have a higher than average density. In addition, the deep-seated model of *Hager et al.* [1985] and *Lithgow-Bertelloni and Silver* [1998] is also different from the geological model of *Burke* [1996] and *Nyblade and Robinson* [1994], which assumes that southern Africa is elevated by a high-temperature anomaly within the upper mantle. These models are apparently inconsistent, and additional constraints on this fundamental problem are required to bound the density of mantle structures. One possible constraint is the excess ellipticity of the core-

mantle boundary (CMB) inferred from geodetic estimates of the period of the Earth's free core nutation. *Forte et al.* [1995] have argued that this anomalous flattening of the CMB is dynamically supported by the low-density antipodal megaplumes beneath southern Africa and the Pacific, thus supporting the view that the density of these seismically inferred features is dominated by their thermal signature. A second constraint involves not only the high topography of southern Africa but also the time history of uplift. If the elevation of Africa is dynamically supported, then it is probably changing as a function of time at a rate that depends on the viscosity and density distribution in the mantle. Here we formulate dynamic Earth models in which we consider not only instantaneous dynamic topography, h, and the geoid but also the rate of change of dynamic topography, $\partial h/\partial t$. This strategy allows us to constrain dynamic models with both present-day residual topography as well as geologic constraints on the vertical motion of the Earth's surface. Our results allow us to place bounds on the density anomaly of the African plume specifically as well as mantle seismic anomalies in general.

2. Mantle Structure Beneath Africa

[6] In general, our view of the Southern Hemisphere, including the region beneath Africa has been improved with a new degree-20 shear wave velocity model (S20RTS) derived by inversion of surface wave phase velocity, body wave travel time, and free-oscillation splitting measurements [*Ritsema et al.*, 1999; *van Heijst et al.*, 1999]. These data cover a wide spectrum of seismic frequencies and simultaneously constrain both long- and short-wavelength seismic velocity variations. We use measurements from digital global and regional seismic network recordings of earthquakes that occurred between 1980 and 1998 to obtain travel times and surface wave data. The surface wave data set contains over a million phase velocity

measurements of fundamental and higher-mode Rayleigh waves for seismic periods ranging from 40 to 250 s. Higher-mode (up to the fourth overtone) phase velocity measurements, which constrain seismic structures in and below the upper mantle transition zone (400–1000 km depth), constitute a unique subset of these data [*van Heijst and Woodhouse*, 1999]. The body wave data set includes nearly 50,000 hand-picked absolute travel time measurements for a large variety of seismic phases that propagate through the lower mantle, including S, S_{diff}, multiple surface reflections (SS, SSS), core reflections (ScS, ScS_2, ScS_3), and core phases (SKS, SKKS). The third type of data used are normal mode structure coefficients for multiplets below 3 mHz. These data, provided to us by J. Resovsky (1999), are a particularly useful constraint on the very long-wavelength (>2000 km) pattern of seismic velocity variation and they complement body wave and surface wave data to provide a constraint on seismic structures in the midmantle [*Resovsky and Ritzwoller*, 1999].

[7] Horizontal and vertical cross sections through model S20RTS illustrate that the low shear velocity anomaly beneath Africa has a complex three-dimensional shape (Figure 1). This anomaly, centered beneath the southeastern Atlantic Ocean, covers an extensive region in the lowermost mantle (4000 km × 2000 km at the CMB) and is connected to patches of low shear velocity beneath central Africa, northwestern Africa, and the southern Indian Ocean. Structures with relatively high shear velocity beneath North and South America, the polar regions, eastern Asia and the Indian Ocean surround the African anomaly. At a depth of 2000 km the low shear velocity anomaly beneath Africa is centered beneath southern Afri-
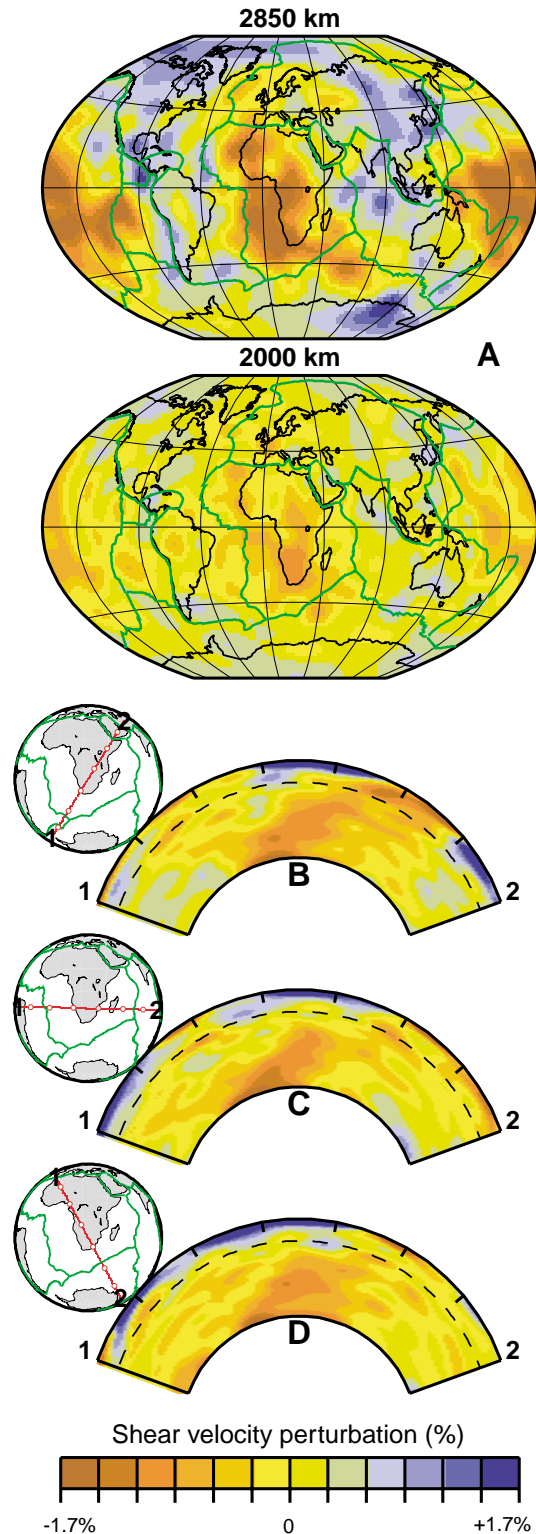

Figure 1. Cross sections through the seismic tomography model S20RTS.

ca and extends over a much narrower region than at the CMB.

[8] Obliquely oriented vertical cross sections (Figures 1B, 1C, and 1D) illustrate that the African low-velocity anomaly extends to a height of 2000 km above the core-mantle boundary, that it tilts in an easterly-northeasterly direction, and that it is possibly connected to a low shear velocity structure in the upper mantle beneath the East African Rift region [*Ritsema et al.*, 1999]. The seismic model S20RTS has similarities to earlier models [*Su et al.*, 1994; *Li and Romanowicz*, 1996; *Masters et al.*, 1996], although it provides higher spatial resolution of mantle shear wave velocity heterogeneity.

3. African Topography and Uplift

[9] Africa has an unusual elevated physiography. Not only does it have the highest elevation for a continent that has not undergone recent compressive tectonism, but it has a distinctive hypsometry reflecting broad scale uplift [*Harrison et al.*, 1983; *Cogley*, 1985]. The southern half of the continent is an extensive plateau at an elevation of ∼1 km (Figure 2). The elevated topography extends from southern Africa through the East African Plateau and the East African Rift Valley [*Burke*, 1996; *Partridge*, 1997] and is continuous with the anomalous bathymetry of the surrounding Atlantic and Indian Ocean basins [*Nyblade and Robinson*, 1994]. Indeed, *Nyblade and Robinson* [1994] referred to the entire region from the south Atlantic mid-ocean ridge to the East African Plateau as the African Superswell. Perhaps most important in the context of this study is that the elevated topography has developed over time. Although estimates of uplift vary widely, most estimates have much of the uplift occurring since the breakup of Gondwanaland with a significant amount occurring during the Cenozoic.

3.1. Topography

[10] In general, much of the Earth's topography, either in the oceans or on the continents, is generated by density variations at relatively shallow depths (<50 km). The contributions of these shallow sources must be removed in order to use topography to infer mantle flow. A map of residual topography for both the oceans and continents, with the mean continental elevation removed from the later (Figure 3) is an important diagnostic tool for understanding anomalous topography. Within the oceans, residual topography is derived by subtracting the normal subsidence of oceanic lithosphere and the effects of sediment loading from observed bathymetry [*Crough*, 1983]. Bathymetry normally increases as $a^{1/2}$, where a is lithospheric age since formation at a mid-oceanic ridge, but tends to flatten for ages greater than about 80 Ma. We believe that the preponderance of evidence concerning the oceanic lithosphere is most consistent with it behaving as a cooling, semi-infinite half space. Oceanic bathymetry does not tend to flatten in a systematic fashion regionally [*Marty and Cazenave*, 1989], as is often presumed, and it is not clear what is causing the bathymetry to shallow. The anomalous bathymetry could, for example, originate from the presence of warmer than average mantle directly beneath the lithosphere or it could result from dynamic support from deep sources of buoyancy. Consequently, only the $a^{1/2}$ term should be removed when generating residual topography maps so that any anomalous bathymetry can be tested against predictions of different geodynamic models.

[11] Following *Pribac* [1991], bathymetry is corrected for conductive cooling using

$$h_r = h_o - (2600 + 220a^{1/2}), \qquad (1)$$

where h_r is residual depth (in meters), h_o is observed bathymetry, and a is age of the oceanic lithosphere (in myr). In addition, we
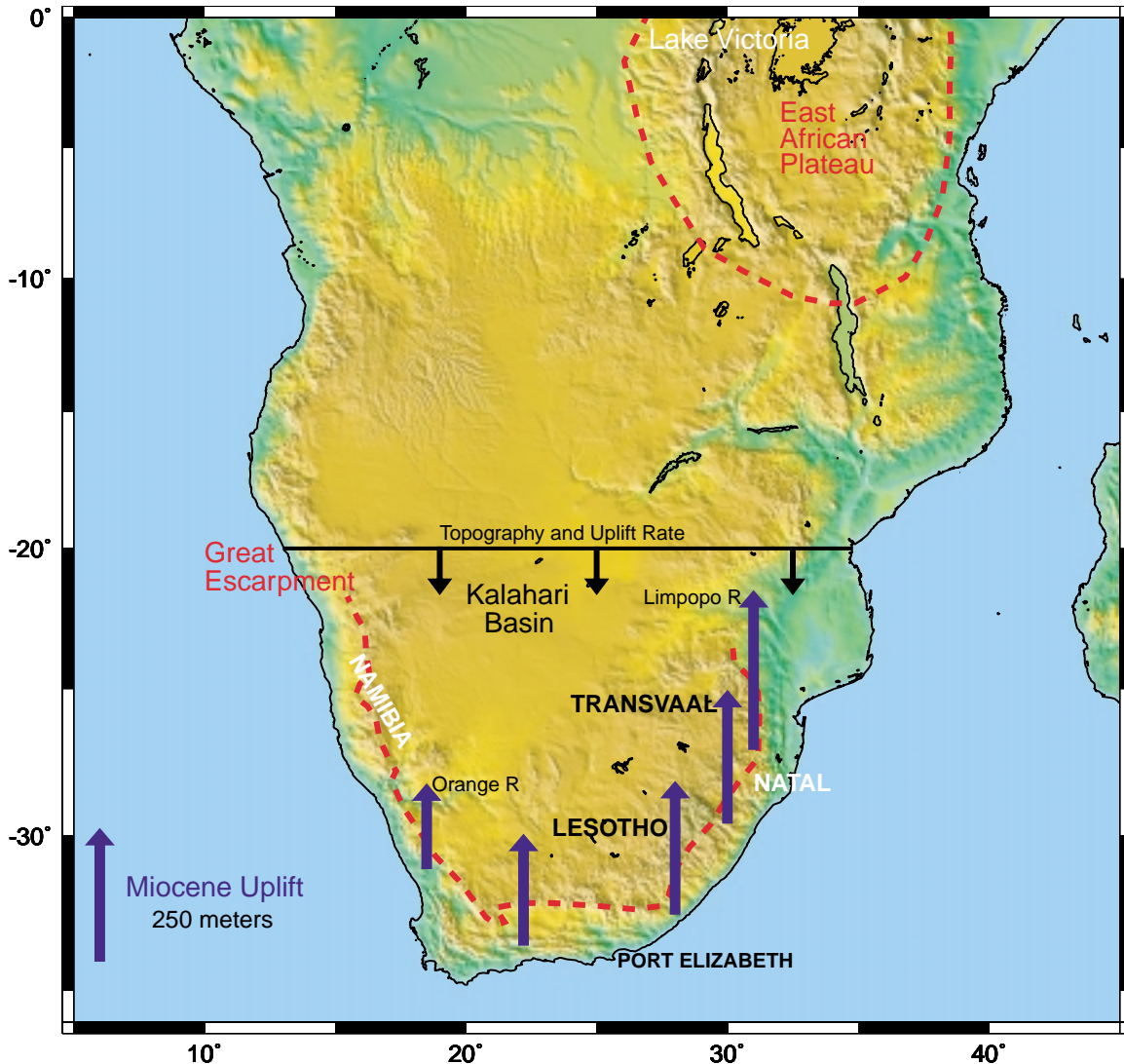
Figure 2. Shaded relief map of southern Africa showing the regions described in the text. The approximate position of the Great Escarpment is shown after *Ollier and Marker* [1985]. Miocene uplift is shown after *Partridge* [1997]. The continental region below the line "Topographic and uplift rate" is used as the region over which averages in dynamic topography and uplift rate are determined in the dynamic models.

correct for sediment loading using the procedure outlined in *Schroeder* [1984] with sediment thicknesses within the ocean basins taken from *Laske and Masters* [1997]. Finally, we add the observed topography of continents reduced by the mean elevation of all continents; this mean value is 565 m [*Harrison et al.*, 1983]. Our procedure and resulting topography

are essentially identical with *Nyblade and Robinson* [1994], but our map provides a global perspective instead of a regional one.

[12] Our map of residual topography (Figure 3) shows a broad region of high topography, approximately 10^7 km^2 in area, which extends from close to the mid-ocean ridge in the South
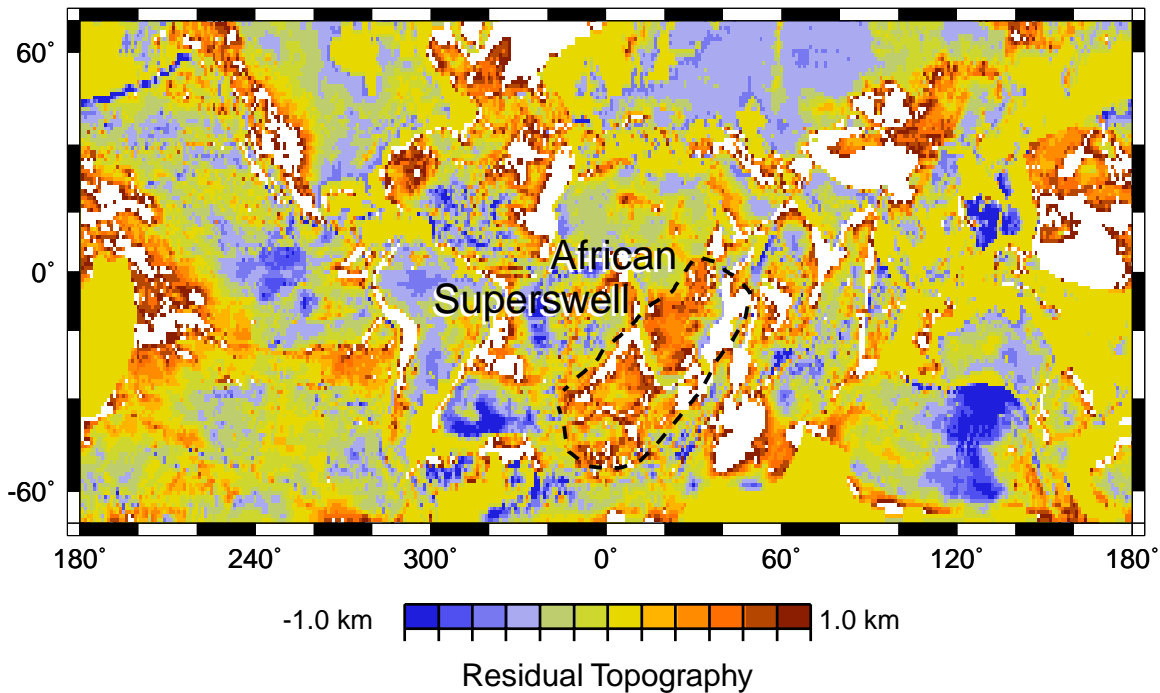
Figure 3. Global residual topography map with polar regions excluded. The map was determined by subtracting the normal subsidence and sediment loading effect from the ocean floor and an average continental elevation. The black dashed line encircles the region described by *Nyblade and Robinson* [1994] as the "African Superswell."

Atlantic through Africa and continuing to equatorial east Africa (the East Africa Plateau). Another uplifted area of comparable dimensions (Figure 3) is located in the central and western Pacific and has been described by *Davies and Pribac* [1993]. This anomaly encompasses both the Darwin Rise and the South Pacific Superswell [*McNutt and Fischer*, 1987]. Other areas of elevated topography evident in Figure 3, such as the Tibetan Plateau and the Andes, are associated with compressive tectonics. Negative residual topography anomalies are located in the back arc regions of the Pacific, the Australian region, and eastern South America.

3.2. Uplift Rate

[13] An important constraint on the origin of the African Superswell comes from the time period over which the topography has been created. Since ours is the first attempt to constrain dynamic mantle models with uplift rate, we will attempt to extract a simple scalar value, the average uplift rate of southern Africa, over the period in which the topography was created. We focus exclusively on southern Africa because of its unique physiography. Eastern Africa also reaches similar elevations as southern Africa and its uplifted topography may have been generated over a comparable period of time. *Partridge* [1997], reviewing the geologic evidence for uplift within the East Africa Plateau, argues that about 300 to 500 m of the 1200-m average elevation may have resulted from doming over the last 20 Myr. Since in east Africa, in contrast to southern Africa, an appreciable amount of uplift has been related to constructional volcanism and rifting (especially rift-

flank uplift) [*Burke*, 1996; *Partridge*, 1997], we restrict our attention to southern Africa. Inferring the timing of uplift from geological observations is difficult and for southern Africa the effect has been the subject of considerable debate. We will attempt to bound the average post-Mesozoic uplift rate of southern Africa from published syntheses that take into consideration the distribution of sediments, offshore sedimentation, the development of land forms, fission track ages, and the tilting of erosional land surfaces.

[14] Raised marine sediments and shoreline deposits provide useful data to estimate uplift. For example, the existence of Cretaceous marine deposits that are hundreds of meters above present sea level is a straightforward means to estimate post-Cretaceous uplift. However, except for some raised Eocene and Cretaceous marine deposits on the coastal plain below the Great Escarpment [e.g., *Maud et al.*, 1987], there are no marine Cretaceous deposits on the southern African plateau [*Sahagian*, 1988]. Both *Sahagian* [1988] and *Burke* [1996] have assumed that such marine deposits once covered southern Africa and have since been eroded away by extensive uplift. This argument is not, in our view, compelling, and in any event does not provide us with a quantitative constraint on the uplift rate.

[15] As an alternative means of estimating uplift, *King* [1962] and *Partridge and Maud* [1987] used ancient surfaces characterized by deeply weathered soil profiles that are typical of the erosional landscape of southern Africa. This method is problematic because of difficulties inherent in correlating surfaces from different regions and placing absolute ages on the erosional surfaces [e.g., *Summerfield*, 1985]. *Partridge and Maud* [1987] attempted to overcome these difficulties with extensive field work in their analysis of the geomorphic evolution of southern Africa, but other workers

remain unconvinced by the robustness of their approach [*Brown et al.*, 2000]. In order to add age constraints, *Partridge and Maud* [1987] correlated terrestrial land surfaces within the interior with dated offshore sequences. Within the interior plateau, where deformation and dissection is poorly developed, sections were formed by correlating surface remnants. *Partridge and Maud* [1987] describe how the oldest of the post-Mesozoic surfaces are characterized by massive laterite or silcreate duricrusts that overlay deeply kaolinized bedrock. Although only present as relics, primarily in the form of erosional mesas, this oldest surface in southern Africa has by far the most widespread distribution. *King* [1962] called this the African surface, and it is indicative of a generally low lying continent, perhaps similar to Australia today [e.g., *Burke*, 1996], forming in a humid environment. The succeeding surface is called Post African [*King*, 1962].

[16] On the basis of geomorphic analyses the relative position of ancient erosion surfaces and offshore sedimentation, *Partridge and Maud* [1987] propose the following uplift history for southern Africa. They argue that the Great Escarpment initiated during the Late Jurassic to Early Cretaceous, following the breakup of Gondwanaland. From Late Jurassic to Early Cretaceous and extending into about the end of the early Miocene the deeply weathered soil profiles of the African surface developed both above and below the Great Escarpment. During the middle Miocene, there was asymmetrical uplift and tilting of the African surface with an amplitude of 150–300 m. This was followed by another period of erosion from the middle Miocene to late Pliocene (Figure 2). A much more significant period of uplift during the late Miocene resulted in a similar overall pattern of asymmetrical uplift and western tilting. The amount of uplift was estimated to range from about 100 to 900 m, with the high values occurring in the east.

[17] In support of the Miocene uplift, *Partridge and Maud* [1987] highlight the elevation of previous coastal and near-shore deposits near Port Elizabeth on the southeast coast of South Africa. They show that the height of Eocene and Cretaceous marine deposits varies linearly with distance from the ocean with a gradient corresponding to the mean gradient of the African surface [*Maud et al.*, 1987]. In addition, *Dingle* [1982] documents a major late Eocene to early Miocene hiatus in the offshore sedimentation rate along the entire margin of southern Africa. This would be consistent with the Miocene uplift proposed by *Partridge and Maud* [1987] if the presently submerged regions were uplifted above sea level. Finally, in a later work, *Partridge* [1997] argued that the profiles of major river systems of the east coast of southern Africa are convex upward, consistent with uplift and warping.

[18] The Great Escarpment (Figure 2) is by far the most prominent feature of southern African physiography. The timing of the uplift associated with the formation of the Great Escarpment is uncertain. It runs almost continuously in a horseshoe-shaped curve from Namibia in the west to the Limpopo River in the east (Figure 2) and separates the high plateau from the more varied lower country for a distance of approximately 3000 km [*Ollier and Marker*, 1985]. *Partridge and Maud* [1987] and others argue that the formation of the Great Escarpment initiated during the breakup of Gondwanaland in the Jurassic when southern Africa was already at high elevations. In contrast, *Burke* [1996] argues that the Great Escarpment is a young feature that formed in response to rapid uplift since 30 Ma. In support of his argument, *Burke* [1996] cites the following evidence. First, the existence of the Oligocene unconformity seen in seismic reflection profiles all around the continental margin suggests rapid uplift initiated at about 30 Ma. Second, the Great Escarpment only occurs along a relatively short length of the entire coastline that was rifted with the breakup of Gondwanaland. Third, preliminary estimates on present-day erosion rates seem to be incompatible with the 50 to 200 km migration of the Great Escarpment after 150 million years. However, recent apatite fission track analysis (AFTA) and thermal history modeling of samples along the Atlantic margin of southern Africa [*Gallagher and Brown*, 1999] demonstrate a pulse of denundation during and following rifting, implying the existence of significant relief during Gondwanaland breakup [*Brown et al.*, 2000]. This high relief is compatible with the hypothesis of high topography along the margin during rifting, but the AFTA neither require nor rule out significant broad-scale uplift occurring after rifting.

[19] We now attempt to estimate the average post Mesozoic uplift rate of southern Africa. A low estimate comes from the tilting of land surfaces believed to originally be part of the African surface, which yields total uplifts of 150 to 300 m. The high values in this range occur in Natal [*Partridge and Maud*, 1987]. These uplifts were thought to occur during and since the Miocene. A lower bound on uplift rate of about 8–17 m/Myr is derived by averaging this uplift over the entire period (∼18 Ma). The timing of this event is derived from the early Miocene hiatus in sedimentation, but the entire duration of this hiatus spanned late Eocene to early Miocene [*Dingle*, 1982]. If the onset of this uplift occurred as early as the middle Oligocene unconformity cited by *Burke* [1996], then the minimum uplift rate is about 5 m/Myr. However, we cannot be certain that the middle Oligocene unconformity is a proxy for regional uplift: It is possible that this unconformity is present globally, suggesting that it may result from a eustatic change in sea level [*Siesser and Dingle*, 1981; *Hallam*, 1992]. Larger rates emerge from the arguments made by *Burke* [1996], who would have south-

ern Africa low lying, as Australia is today, before 30 Ma. For the high plateau of southern Africa this amounts to uplifts of about 400 to 800 m at rates of 13–27 m/Myr. Burke's argument is plausible but appears to be inconsistent with the AFTA along the margin that requires a Jurassic pulse in denudation during Gondwanaland breakup. *Partridge and Maud* [1987] also estimate a late Neogene uplift with a maximum value of about 900 m in Natal, but with substantially smaller values throughout most of South Africa (∼100 to 200 m occurring perhaps since the Pliocene). This yields uplift rates of 30–80 m/Myr over southern Africa albeit that such rates could not have been sustained over a long period of geologic time. The evidence for this uplift appears to be limited and based on Post African surfaces that are difficult to correlate.

[20] In summary, within southern Africa uplift rates of 5–30 m/Myr over much of the Cenozoic appear to be consistent with a range of observations and geological arguments. We must be open to the possibility that there may have been no uplift since Gondwanaland breakup (that is, that the high topography is a relic of processes causing a permanent change in continental elevation before breakup [*Summerfield*, 1996; *Brown et al.*, 2000]). However, we consider this latter interpretation to be less plausible given both the broad scale extension of the topographic high that characterizes southern Africa into the South Atlantic Ocean [*Nyblade and Robinson*, 1994] (Figure 3) and that southern Africa does not have an anomalously thick crust [*Mooney et al.*, 1998]. Furthermore, while we do not consider the evidence in support of a rapid Pliocene uplift robust, we will consider the implications of this hypothesis within the context of a range of geodynamic models. Within a region where the uplift of the land surface is primarily epeirogenic, the continental area south of 20°S (Figure 2), the mean residual topography, derived from our analysis

above, is 452 m; we consider a plausible range to be 300–600 m.

3.3. Geoid

[21] Estimating the geoid anomaly associated with southern Africa is problematic. The non-hydrostatic geoid [e.g., *Hager et al.*, 1985] is positive at long wavelengths over southern Africa, but from the shape of the field, there is no compelling reason to believe that part of the signal is localized there. The height of the geoid in southern Africa is 20–30 m [*Marsh et al.*, 1990]. Comparing our predictions to this range may not be appropriate since the geoid could well be controlled by long-wavelength structure unrelated to the structure and flow beneath southern Africa. Nevertheless, we use this approach and show that plausible dynamic models are consistent with this range of values.

4. Model Formulation

[22] The topography and geoid that result from mantle flow models constrained by seismic tomography have been considered in a number of studies [e.g., *Hager et al.*, 1985; *Lithgow-Bertelloni and Silver*, 1998]. These studies generally used an analytic formulation in which boundary deflections, including surface topography, resulted from instantaneous Stokes flow within a sphere with radially stratified viscosity. In order to compute the rate of uplift, which we define as the time derivative of surface dynamic topography, we must solve for the coupled system of flow and advection of the density field. Consequently, we formulate this computation in a manner akin to the solution of a classical problem in convection in which the equations of motion and energy are coupled [e.g., *McKenzie et al.*, 1974].

[23] The mantle is treated as an incompressible, viscous fluid in which inertial forces are neg-

ligible. The dynamics are governed by the nondimensional continuity, momentum, and transport equations:

$$u_{i,i} = 0, \tag{2}$$

$$-P_{,i} + (\eta u_{i,j} + \eta u_{j,i})_{,j} + Ra\delta\rho\delta_{ir} = 0, \tag{3}$$

$$(\delta\rho)_{,t} + u_i(\delta\rho)_{,i} = (\delta\rho)_{,ii}, \tag{4}$$

where u_i is the velocity, P is the dynamic pressure, $\delta\rho$ is the density, g is the acceleration of gravity, η is the dynamic viscosity, i and j are spatial indices, t is time, and δ_{ir} is the Kronecker delta. In (3), Ra is the effective Rayleigh number, which we define as

$$Ra = \frac{\rho_o g R_o^3}{\eta_o \kappa_e}, \tag{5}$$

where R_o is the radius of the Earth, ρ_o is the reference density, η_o is the reference viscosity (assumed to be the upper mantle value), and κ_e is an effective diffusivity. If the density differences within the mantle were purely thermal, then κ_e would be the thermal diffusivity as it normally appears in the Rayleigh number. If the density differences in the mantle are purely chemical in origin (highly unlikely since the mantle is a heat engine), then κ_e would be considerably smaller than the thermal diffusivity. However, since a finite κ_e is required to ensure numerical stability, we assume that κ_e is the thermal diffusivity. Since the major objective of this paper is the use of uplift rates, this assumption has no influence on our results since the (nearly) instantaneous uplift rate will be controlled by the advection of density differences.

[24] We consider two types of numerical models. First, to identify sensitivities associated with predictions of dynamic topography, uplift rate, and geoid, we perform a large suite of calculations in which (2)–(3) are cast in a stream function - vorticity formulation and solved on an axisymmetric finite difference grid extending from the symmetry axis out to

Table 1. Summary of Controlling Parameters

Parameter	Symbol	Value
Radius of the Earth	R_o	6371 km
Acceleration due to gravity	g	10 m s^{-2}
Reference density	ρ_0	3300 kg m^{-3}
Effective diffusivity	κ_e	10^{-6} m^2 s^{-1}
Reference viscosity	η_o	10^{21} Pa s
Reference shear velocity	$\overline{\beta}$	6.5 km s^{-1}
Effective Rayleigh number	Ra	8.5 × 10^9

an angular distance of 90°. The stream function and vorticity equations are solved using MUDPACK routines [*Adams*, 1989], while the advection of density anomalies (4) is solved with a direct method [*Press et al.*, 1992]. Although the code was designed to incorporate both compressibility and temperature-dependent viscosity, the calculations reported here assume incompressibility using the parameters in Table 1 and depth-dependent viscosity.

[25] Second, we map the seismic shear velocity model in section 2 into density anomalies, which are then input into a fully spherical, finite element solution of the equations of motion and transport. This spherical finite element model allows us to explore how temperature-dependent viscosity and lateral variations in lithospheric thickness influence topography and uplift rate. In this case, equations (2)–(4) are solved with CitcomS [*Zhong et al.*, 2000], which is a fully spherical code modified from the finite element method described by *Moresi and Gurnis* [1996]. A mixed method is used to solve for both velocity and pressure. For the momentum equation (3) a multigrid iterative solver is used on a parallel computer. A streamline upwind Petrov-Galerkin method is used to solve the transport equation [*Brooks*, 1981]. For all of the results presented here the mesh consisted of nearly 4.0 × 10^5 trilinear, eight-node elements; the elements were uniformly distributed in radius, and in map view each element covered nearly an equal area (see *Zhong et al.* [2000]).
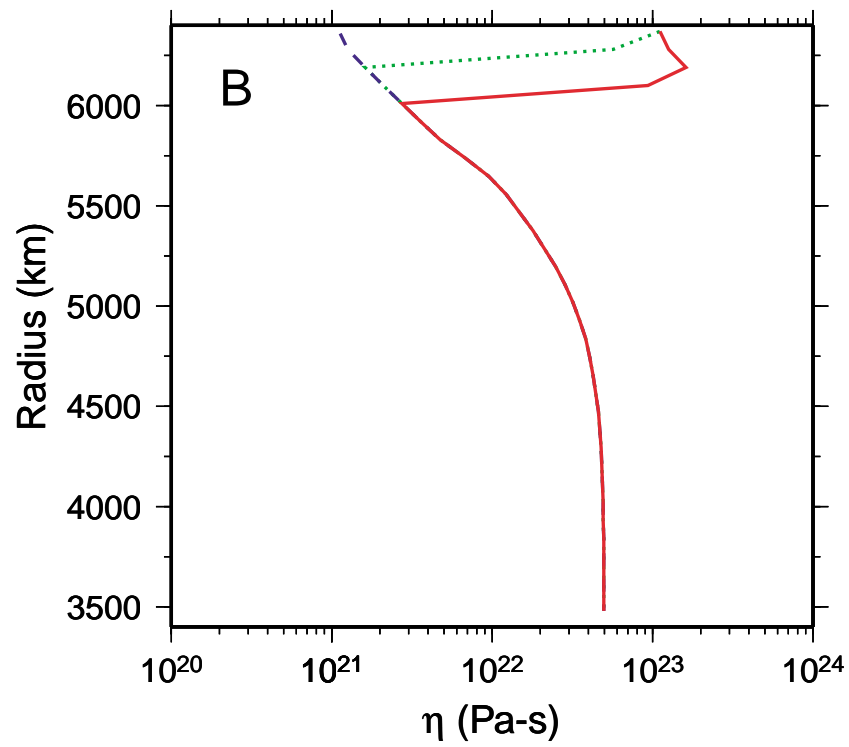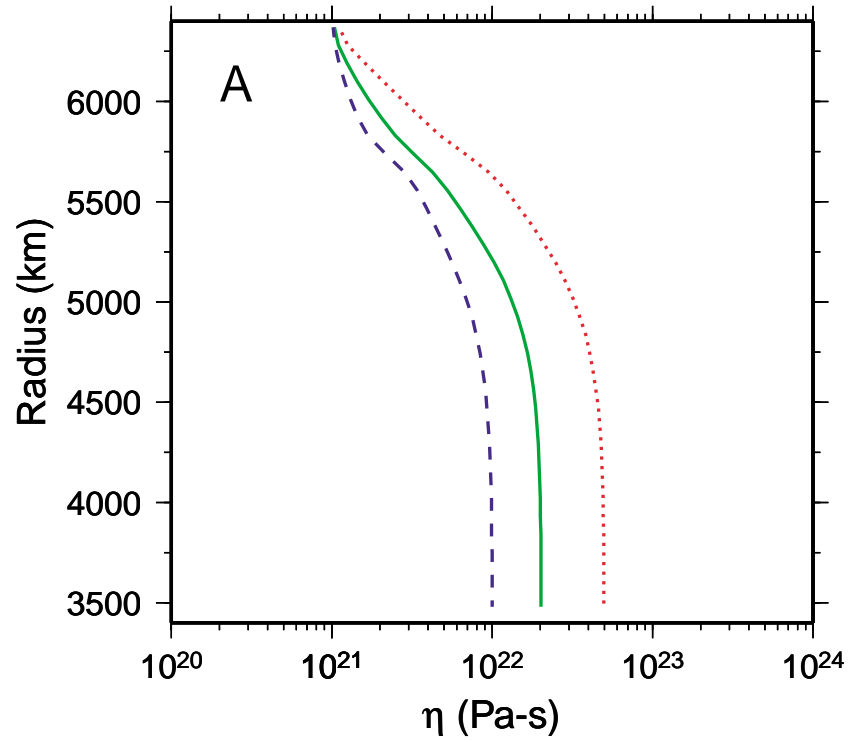
Geochemistry
Geophysics
Geosystems

G^3

GURNIS ET AL.: AFRICAN SUPERPLUME

1999GC000035

Table 2. Summary of Dynamic Earth Models

Case	Domain[a]	Viscosity[b]	$\partial\rho/\partial v_s$, kg m^{-3}/km s^{-1}	$\delta\rho_{peak}$, %	$\langle h \rangle$, m	$\langle \partial h/\partial t \rangle$, m/Myr
1	G	Z50	400	−0.99	1427	11.6
2	G	Z10	400	−0.99	1531	60.2
3	G	Z50	200	−0.49	714	2.9
4	G	Z50	100	−0.24	356	0.72
5	G	Z50	50	−0.12	178	0.18
7	G	Z20	100	−0.24	365	1.7
8	G	Z10	100	−0.24	383	3.8
9	G	Z10+T1	100	−0.24	416	9.1
10	G	Z50+T1	100	−0.24	366	1.6
11	G	Z50+T2	100	−0.24	316	3.4
12	R	Z50	100	−0.24	351	1.3
13	R	Z50+T1	100	−0.24	409	2.2
14	R	Z50+L1	100	−0.24	396	1.3
15	R	Z50+L1+T2	100	−0.24	456	3.3
16	R	Z50+L2+T2	100	−0.24	473	2.5
17	R	Z50+L2+T3	100	−0.24	465	2.2
18	G	Z50	S1	−1.00	621	4.6
19	R	Z50	S1	−0.97	588	5.8
20	R	Z50	S2	−0.90	893	12.1
21	R	Z50+T2	S2	−0.90	1145	29.1
22	R	Z50+L2+T2	S2	−0.90	1496	20.6
23	R	Z50+L2+T2	S3	−0.45	811	6.9
24	R	Z50+L2+T2	S4	−0.45	718	3.4

[a]G, global; R, regional (solved globally but $\delta\rho$ within latitude: 50° N to 50° S, longitude: 30° W to 70° E)
[b]Viscosity: The symbols denote the following characteristics of variable viscosity. Z10, Z20, and Z50 refer to increases in viscosity between the surface and the CMB of 10, 20, and 50, respectively using (9)−(11). L1 and L2 refer to lithospheric lids with thicknesses of 150 and 271 km, respectively. T1 to T3 have the same temperature-dependent parameters (γ=1.97, T_o=0.5, E=115.075, and η^*=2.194 × 10^{-17}); for T1, T2, and T3 the temperature-dependent viscosity occurs below 660, 200, and 170 km, respectively.

[26] Benchmarks for CitcomS were presented by *Zhong et al.* [2000], but we also carried out additional benchmarks in which topography, uplift rate, and flow velocity obtained using the model were compared with results for the axisymmetric code. In particular, we considered predictions for a nearly spherical plume described in section 5 using a radially stratified viscosity profile with an order of magnitude change between the upper and lower mantle (Figure 4). Comparisons between the finite difference and finite element model show that the dynamic topography, uplift rate, and flow velocity agreed to within 1%.

[27] A simple linear scaling is used to obtain density from shear wave perturbations that arise from seismic inversions

$$\delta\rho = \frac{1}{\rho_o}\left(\frac{\partial\rho}{\partial v_s}\right)\overline{\beta}\delta v_s, \qquad (6)$$

Figure 4. Radial viscosity models used in the calculations. (A) Simple smooth depth dependent models characterized by a viscosity increase from the surface to the CMB of 10 (blue, dashed), 20 (green, solid), and 50 (red, dotted). The profiles have the analytic form (9)−(11), with the following values for (η_3, η_2, η_1, β_η): Red dotted line, (200, 2, 1, 0.245); solid green line, (29, 2, 1, 0.705); blue dashed line, (11.5, 2, 1, 0.845). (B) Models identical to the red, dotted line in Figure 4A but with different lids; no lid (blue, dashed), 150-km-thick lid, which is 100 times more viscous than the upper mantle (green, dotted), and 271 km thick with the same viscosity contrast (red, solid).

where $\delta\rho$ is the nondimensional density perturbation, δv_s is the nondimensional shear wave perturbation, $\bar{\beta}$ is the reference shear velocity in the lower mantle, and $\partial\rho/\partial v_s$ is the shear wave to density scaling that can be depth dependent. Above a depth of 660 km, $\delta\rho=0$ because much of the seismic velocity variations in the upper mantle associated with continental roots are probably neutrally buoyant [Jordan, 1975]. Without this assumption, continents would be associated with downwellings, and there would be a strong correlation between geoid lows and continents, a correlation that is not observed [Jordan, 1975].

[28] Lateral variations in viscosity have an important influence on dynamic topography [Moresi and Gurnis, 1996; Zhong and Davies, 1999]. Consequently, we expect that lateral viscosity variations will have an important influence on uplift rate as well. We employ a viscosity that is exponentially dependent on seismic shear velocities. This translates into temperature-dependent viscosity if, indeed, the seismic shear velocities are purely thermal in origin. Viscosity varies as

$$\eta = \eta^* \eta(r) \exp\left(\frac{E}{T_{\text{eff}} + T_o} - \frac{E}{1 + T_o}\right), \qquad (7)$$

where η^* is a constant. T_{eff} is the effective temperature, defined as

$$T_{\text{eff}} = 0.5 + \gamma \delta v_s, \qquad (8)$$

where γ is a constant. The temperature-dependent parameters are given in Table 2. The form of this equation was chosen so that viscosity variations can change independently of $\delta\rho$. The depth-dependent component of viscosity, $\eta(r)$, is defined as

$$\eta(r) = \beta_\eta[\eta_3 + (\eta_2 - \eta_3)\chi_1(r) + (\eta_1 - \eta_2)\chi_2(r)], \quad (9)$$

where

$$\chi_1(r) = 0.5\left[1.0 - \tanh\left((5170.0 - r)\frac{5.0}{d_M}\right)\right] \qquad (10)$$

$$\chi_2(r) = 0.5\left[1.0 - \tanh\left((5703.0 - r)\frac{50.0}{d_M}\right)\right] \qquad (11)$$

In (9)–(11), r is the (dimensional) radius, and d_M is the thickness of the mantle. The forms (10) and (11) are adopted from Richter [1973] and Solheim and Peltier [1993]. The predictions described below use three different radial viscosity profiles specified by the parameters β_η, η_3, η_2, and η_1 (Figure 4A). These profiles are characterized by viscosity contrasts of 10, 20, and 50 from the surface to the CMB (Figure 4A). The parameter β_η is chosen to pin the viscosity at the top of the upper mantle to 1.0 (or a dimensional value of 10^{21} Pa s). Finally, in some models these simple profiles are augmented with a High-viscosity lid (Figure 4B).

5. Some Simple Examples of Uplift Rate, Topography, and the Geoid

[29] Both dynamic topography, h, and uplift rate, $\partial h/\partial t$, increase with the density anomaly driving the flow. Dynamic topography is directly proportional to the density anomaly. Since uplift rate is proportional to the product of dynamic topography and fluid velocity, it will be proportional to the square of the density. Although dynamic topography is sensitive to the radial and lateral variations in viscosity, it is independent of the reference viscosity. Moreover, since flow velocities are inversely proportional to the reference viscosity, uplift rates will be inversely proportional to the reference viscosity. Consequently,

$$\frac{\partial h}{\partial t} = \frac{C}{\eta_o} h^2, \qquad (12)$$

where C is a function of the density and viscosity distributions and can be found by explicit solution of (2)–(4) in which the density anomalies and viscosity distribution are specified. To identify the relationship

between dynamic topography, uplift rate, and geoid, (2)–(4) were solved in an axisymmetric geometry.

[30] The nearly instantaneous ascent of a plume located near the base of the mantle is determined. A plume geometry is established by centering an ellipsoidal structure on the pole of axisymmetry. Let us assume that the center of the plume is located at radius $r = r_{mid}$ and colatitude $\theta = 0$. We denote the maximum half width of the plume in the radial direction on the pole of symmetry to be Δr, and in the θ direction on the sphere $r = r_{mid}$ to be L. The geometry of the density anomaly associated with the plume is then defined as

$$\delta\rho(\theta, r, t = 0) = \Delta\rho\left[1 - \left(\left(\frac{r-r_{mid}}{\Delta r}\right)^2 + \left(\frac{\theta}{\theta_{cut}(r)}\right)^2\right)\right] \quad (13)$$

when $r_{mid} - \Delta r \leq r \leq r_{mid} + \Delta r$, $\theta \leq \theta_{cut}(r)$, and the quantity in square brackets on the right-hand side of (13) is greater than zero. When these conditions fail to hold, $\delta\rho(\theta, r, 0) = 0$. The parameter $\theta_{cut}(r)$ is simply related to the maximum half width at $r = r_{mid}$ by:

$$\theta_{cut}(r) = \frac{L}{r.} \quad (14)$$

[31] The dimensions of our model plume were chosen to provide a rough match to the spatial scales of the velocity anomaly at the base of the mantle under Africa (Figure 1). Specifically, we used values of $r_{mid} = r_{cmb} + 900$ km, $\Delta r = 600$

km, and $L = 1000$ km. With this geometry the free parameters of the model are the peak density anomaly $\Delta\rho$ and the mantle viscosity profile. For the plume geometry given by (13) the mean density anomaly within the plume is roughly one-half the peak value.

[32] We first explore the relationship between dynamic topography and uplift rate driven by the ascent of the model plume (Figure 5A). Each line on Figure 5A joins results obtained using a specific mantle viscosity profile. The small open circles on each line refer to calculations with different peak density anomalies; specifically, from left to right, $\Delta\rho/\rho_o = -0.2\%, -0.4\%, -0.6\%,\ldots, -2.0\%$ (having mean density anomalies ranging from -0.1 to -1.0%). These results indicate that the uplift rate increases with the square of the dynamic topography. Indeed, a 10-fold increase in the density anomaly leads, for all three viscosity profiles, to a 10-fold increase in dynamic topography and a 100-fold increase in uplift rate (Figure 5A). Furthermore, an increase in the deep mantle viscosity by a factor of 10 decreases the predicted uplift rate by nearly an order of magnitude (when results using the same $\Delta\rho/\rho_o$ are compared). Thus our heuristic result relating topography to uplift rate is verified by these calculations.

[33] These scaling arguments and the results in Figure 5A raise several important points.

Figure 5. (A) Predictions of uplift rate versus dynamic topography for a suite of simulations in which both the mantle viscosity profile and the peak density anomaly of the plume is varied. Each line joins results obtained using the same viscosity profile. For example, the solid line in the frame is based on the viscosity profile denoted by the solid line in Figure 4, and so on. The numerical labels in Figure 5A refer to the increase in viscosity (10-fold, 20-fold, etc.) from the top of the upper mantle to the core-mantle boundary (CMB) associated with the simulations. The small open circles connected by each line refer to model runs with (from left to right) progressively greater plume buoyancy. In particular, we show results for peak plume density anomalies of $-0.2, -0.4,\ldots, -2.0\%$ (or mean plume density anomalies ranging from -0.1 to -1.0%). The box represents our estimate of the observational constraints on the uplift history of southern Africa (see text). (B) As in Figure 5A, except for the uplift rate versus geoid. (C) As in Figure 5A, except for the geoid versus dynamic topography.

Dynamic Topography
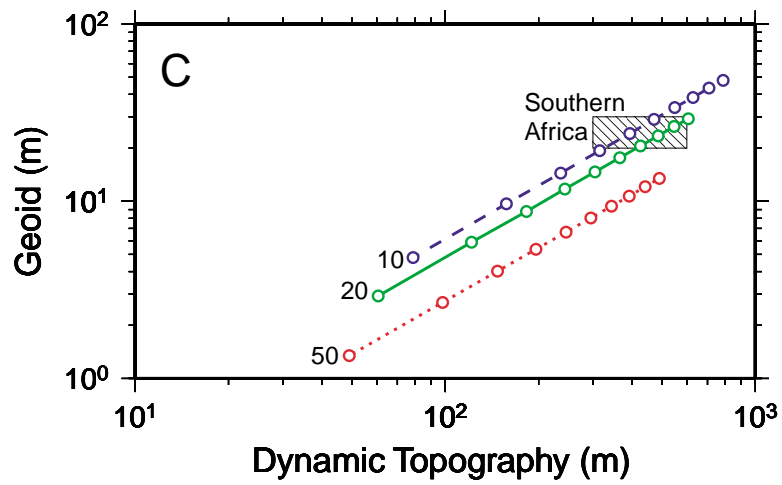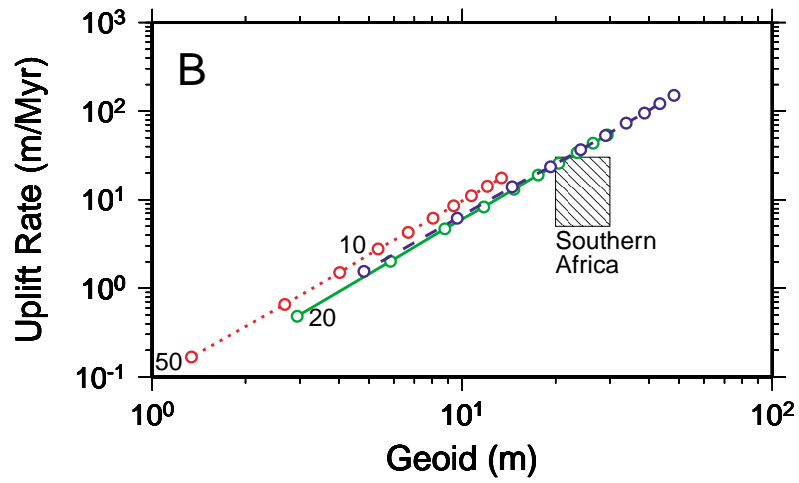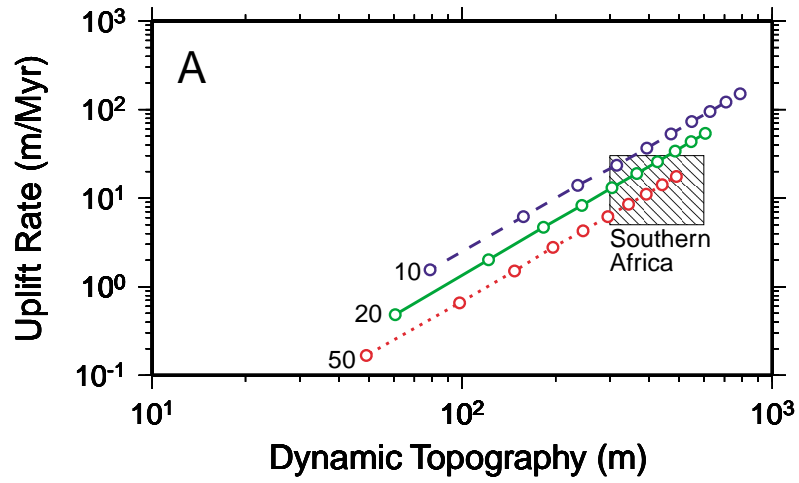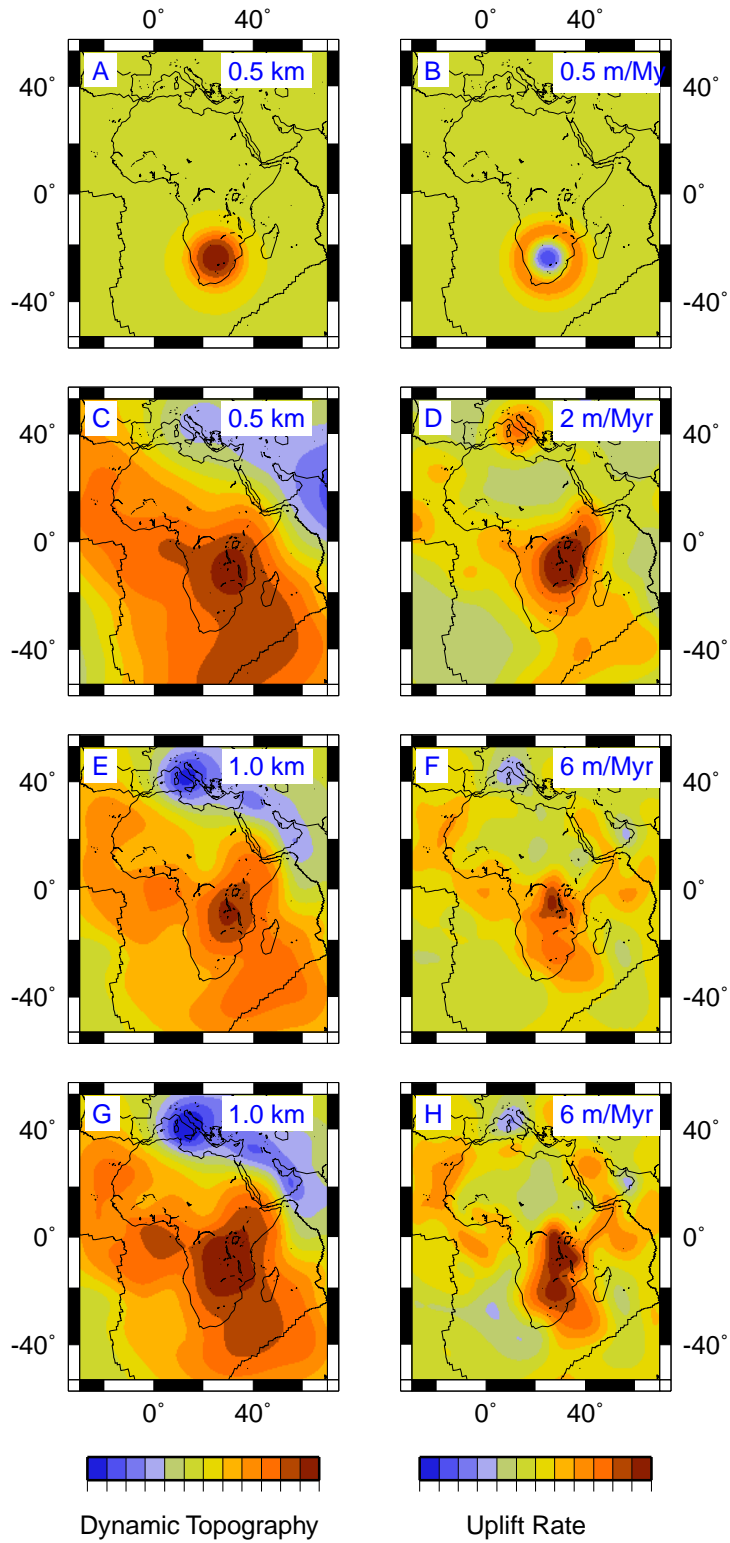
Uplift Rate

First, increasing the density of the ascending plume has a larger effect on the uplift rate than the dynamic topography. Second, varying the mantle viscosity, for a given plume, has a stronger influence on the uplift rate than the dynamic topography. Indeed, decreasing the lower mantle viscosity by a factor of 10 increases the uplift rate by roughly the same amount and the dynamic topography by approximately a factor of 3. The difference in sensitivities will be a function of the details of the viscosity profile. Nevertheless, these results demonstrate that robust estimates of uplift rates provide a potentially important constraint on plume density and mantle viscosity.

[34] Our theoretical plume model also allows the canonical geological model, apparently inconsistent with shear wave inversion for southern Africa (Figure 1) (a low-velocity, low-density anomaly directly under the continental Lithosphere) to be explored. Using (13) with $\Delta r = 200$ km and $L = 1500$ km at 300-km depth (equivalent to a lens-shaped anomaly under the lithosphere) and $\Delta \rho = 0.17\%$, a peak dynamic topography of 500 m is obtained (Figure 6A). The anomaly is shifted to southern Africa while using the spherical finite element method. With this density configuration the time rate of change in topography is small, as the structure is nearly in isostatic equilibrium. The uplift rate has a morphology in which higher-amplitude subsidences are encircled by positive uplifts (Figure 6B). This distinctive surface expression results from vertical fluid velocities that are smaller than the horizontal (radially outward from the center of the plume), so that the plume thins while growing in radius [e.g., *Griffiths et al.*, 1989].

6. Application to the African Region

[35] We have carried out a series of calculations (summarized in Table 2) using the finite element method to explore how actual mantle density distributions, inferred from our shear velocity model, are manifest in topography and its rate of change within southern Africa. To begin, consider our case 1, which adopted parameters typical of those used in earlier studies of the geoid and dynamic topography. The model has a factor of 50 increase in viscosity from the upper to the lower mantle with $\partial \rho / \partial v_s = 400$ kg m^{-3}/km s^{-1}. This velocity to density scaling gives rise to $\approx 1\%$ peak-to-peak variations in density (Table 2, Figure 7). A great circle section through the mantle shows the African anomaly as well as a nearly antipodal slow anomaly in the central Pacific. In cross section, between these low shear wave velocity regions, there are two substantial high-velocity regions (one beneath Central America, the other beneath the Indonesian archipelago). The cross section demonstrates how the seismic velocity has been converted to density for use with the dynamic model: $\delta \rho$ has been set to zero both at the CMB and above a depth of 660 km. The resulting dynamic topography, shown in Figure 8 (middle), is typical of those that have been published in the past [*Hager et al.*, 1985; *Lithgow-Bertelloni and Silver*, 1998]: Dynamic topography highs are associated with Africa, especially southern Africa and the central Pacific, while dynamic topography lows are centered over Indonesia/western Pacific and South America. The amplitude of the topography is large, ≈ 2500 m (Figure 8, middle).

[36] The predicted uplift rate has a regular pattern that is correlated with the strong lower

Figure 6. Regional maps of (left) dynamic topography and (right) surface uplift rates for four different models: (A−B) a shallow, flattened plume head directly beneath the lithosphere (details given in the text), (C−D) case 4, (E−F) case 16, and (G−H) case 24. The maximum +/− scale for each plot is indicated at the top right.
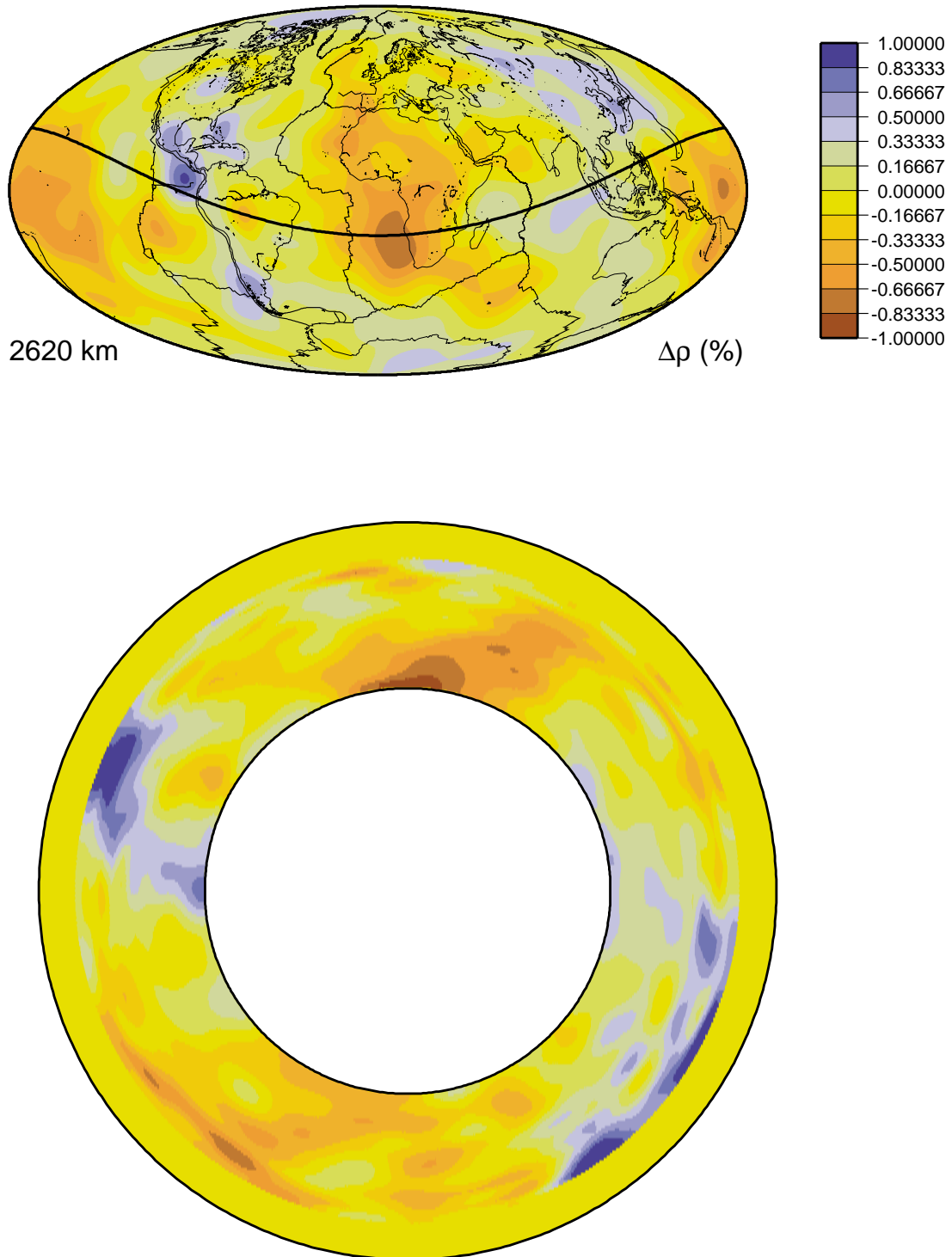
Figure 7. Map of the density anomalies used for case 1 at a depth of 2620 km along with a great circle cross section as indicated. A uniform $\partial\rho/\partial v_s$=400 kg m^{-3}/km s^{-1} has been used to map shear velocity into density.
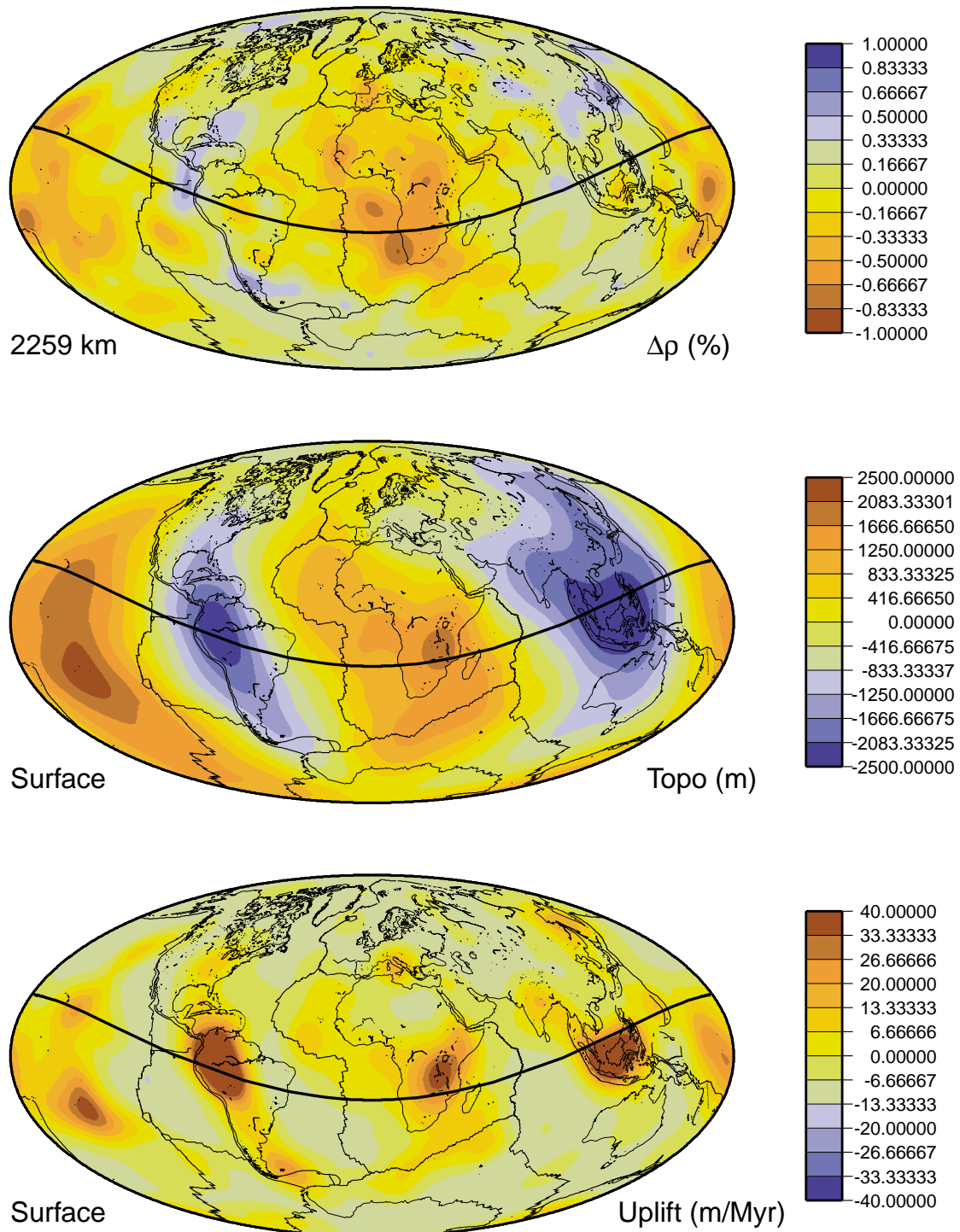
Figure 8. Density anomaly at (top) 2259 km depth, (center) the surface dynamic topography, and (bottom) surface uplift rate for case 1 described in the text. The density anomaly in cross section along the great circle indicated in the maps is shown in Figure 7.
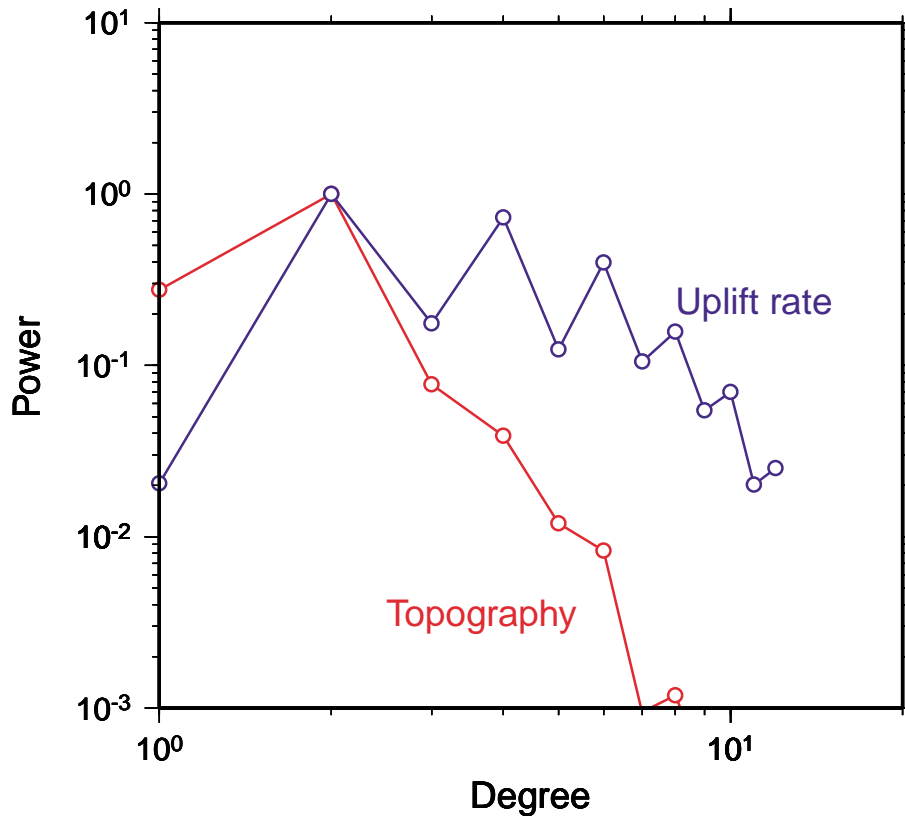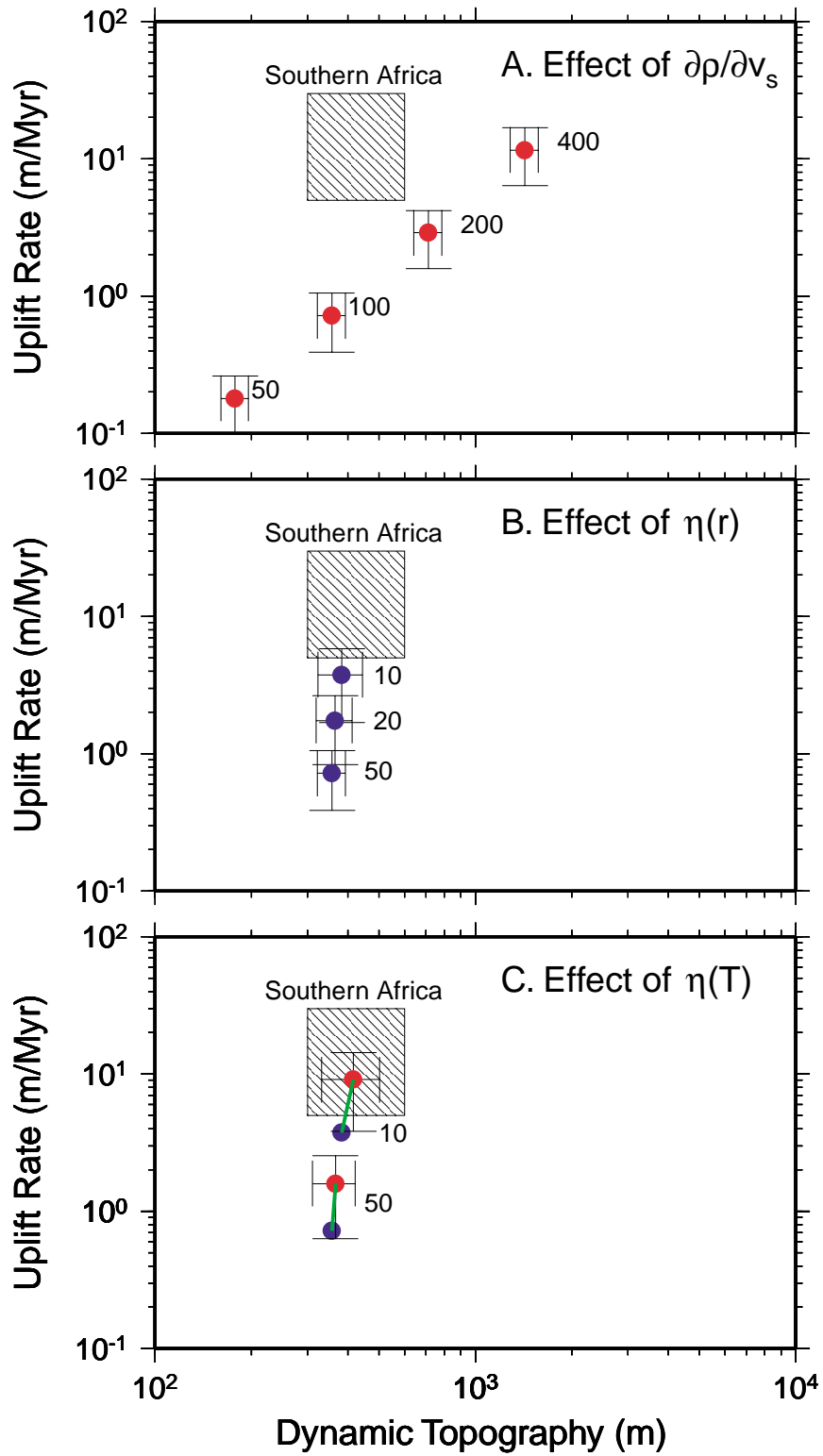
Figure 9. Power spectrum of dynamic topography and surface uplift rate for case 1. Both curves have been normalized by the peak value that occurs at degree 2.

mantle density anomalies (Figure 8, bottom). Uplift rate is predominately uniform with values near zero although strong positive uplift rates are associated with the highs and lows of dynamic topography. The deep-seated low-density anomalies are associated with dynamic topography highs. As described for a generalized spherical anomaly, these low-density structures rise upward, and, as they approach the surface, the amplitude of the dynamic topography increases and results in a positive rate of uplift. The deep-seated high-density anomalies are also associated with positive uplifts; this result seems counterintuitive, but it is physically real and results from a numerically convergent solution. The high-density structures produce dynamic topography lows. As these structures sink deeper into the lower

mantle and thus recede from the top surface, the magnitude of the dynamic topography lows decrease, resulting in a positive uplift rate. The depth distribution of the high-density structures is not realistic because we have removed all anomalies above 660 km depth. In the Earth, these high-density anomalies are connected to upper mantle slabs, and so the rate of uplift will generally be smaller than computed here; indeed, there will be a more or less continuous flux of dense material from the surface (i.e., subduction of cold, dense oceanic lithosphere). In this case, either positive or negative uplifts are possible, depending on how the buoyancy flux (proportional to the product of age of the subducting lithosphere and its convergence rate) varies as a function of time [*Lithgow-Bertelloni and Gurnis*,

A. Effect of $\partial\rho/\partial v_s$

Southern Africa

B. Effect of $\eta(r)$

Southern Africa

C. Effect of $\eta(T)$

Southern Africa

1997]. It is beyond the scope of the present study to deal in detail with the Downwellings, and we will focus on the African structure alone. The uplift rate anomalies shown in the maps are of smaller length scale than dynamic topography anomalies; the uplift rate anomalies are confined to the center of long-wavelength dynamic topography swells. Density anomalies within the lower viscosity portions of the lower mantle rise fastest (Figure 4A) and result in higher (positive) uplift rates. The surface uplift rate field has a broader spectrum compared to the dynamic topography (Figure 9). Although the power spectrum of both dynamic topography and uplift rate peak at degree 2, topography decays faster with smaller wavelengths.

[37] The predicted dynamic topography and uplift rate in Africa for case 1 is centered south of Lake Victoria, just south of the East Africa Plateau [*Partridge*, 1997]. The maximum dynamic topography is approximately 1800 m and the uplift rate is about 20 m/Myr. The high uplift rates are being driven by the low-density (low shear velocity) structure directly underneath this region between 1000- and 2000-km depth (Figure 1B). The seismic anomaly within the lowest 1000 km of the mantle directly beneath southern Africa contributes less to surface dynamic topography and uplift rates. This is expected because the ascent rate will be less when the density anomaly is closer to the bottom (higher viscosity portion; Figure 4A) of the fluid mantle.

6.1. Density Scaling

[38] The dynamic topography $\langle h \rangle$ and uplift rate $\langle \partial h / \partial t \rangle$ are found by averaging over the southern African region (south of 20°S latitude, Figure 2). The trend predicted for a set of models in which the amplitude of the density anomalies varied while the radially symmetric viscosity is held constant (to the profile adopted in case 1), confirms the results of the previous section, in which uplift rate is directly proportional to the square of the dynamic topography (Figure 10A). We note that regardless of the amplitude of the density anomaly, this viscosity profile does not yield solutions acceptable for southern Africa (Figure 10A). All models that produce a good fit to the observed residual topography underpredict the uplift rate by nearly an order of magnitude.

6.2. Depth-Dependent Viscosity

[39] By decreasing the viscosity of the lower mantle, while holding the driving force constant with $\partial \rho / \partial v_s = 100$ kg m^{-3}/km s^{-1} (see Figure 6C and 6D for the case with a factor of 50 increase in viscosity from the surface to CMB), the uplift rate can increase substantially with only a relatively small increase in dynamic topography (Figure 10B). The uplift rate, proportional to the ascent rate of the anomalies through the lower mantle, increases as a function that is nearly inversely proportionally to the viscosity of the lower mantle, while the dynamic topography only increases by a small amount (Figure 10B). This suite of

Figure 10. Dynamic topography versus uplift rate within southern Africa computed from global models for various densities and viscosity structures. (A) Predictions for $50 < \partial \rho / \partial v_s < 400$ kg m^{-3}/km s^{-1} for the radial viscosity profile with a $50 \times$ increase from surface to CMB (cases 5, 4, 3, 1). (B) Predictions for $\partial \rho / \partial v_s = 100$ kg m^{-3}/km s^{-1} for viscosity profiles with $10 \times$, $20 \times$, and $50 \times$ increases from the surface to CMB (cases 8, 7, and 4, respectively). (C) Influence of temperature dependent viscosity. The blue dots are for the purely depth-dependent cases (4, 8) connected via the green line to the corresponding cases with both depth- and temperature-dependent viscosity (respectively, 10 and 9).

calculations indicates that the observed residual topography and uplift rates can nearly be satisfied with a dynamic model. Acceptable models in this regard require a density anomaly that averages ~0.2% and a viscosity structure that increases by about 1 order of magnitude or less from the upper to the deeper lower mantle. This viscosity increase is insufficient to satisfy the constraint implied by positive geoid anomalies above subduction zones that have viscosity increases from the upper to lower mantle of ~30 [*Hager*, 1984].

6.3. Temperature-Dependent Viscosity

[40] The influence of temperature-dependent viscosity is substantial and offers a route to reconcile our prefered models with previous viscosity inferences. For Africa, which overlies an upwelling, temperature-dependent (that is, seismic shear velocity) viscosity decreases the viscosity within the lower mantle beneath the continent (Figure 11); this leads to a substantial increase in uplift rate while only increasing the dynamic topography by a relatively small amount (Figure 10C). The influence on dynamic topography and uplift rate mimics the overall trend evident in purely radial models when lower mantle viscosity decreases (Figure 10B). However, with the temperature-dependent case a strong radial increase in viscosity with depth results beneath subduction zones from the upper to lower mantle (Figure 11).

[41] With the combination of temperature- and depth-dependent viscosity (case 9) and a uniform $\partial\rho/\partial v_s$=100 kg m^{-3}/km s^{-1} scaling through the mantle we are able to obtain average uplift rates and dynamic topographies that fall within the acceptable range of observed values (Figure 10C). These cases have an overall geometric pattern that is not unlike that for a case with purely depth-dependent viscosity (Figure 6C and 6D) in which peak

values in both topography and its rate of change occur just south of the East African Plateau and with substantially smaller values in southern Africa. However, this predicted pattern of dynamic topography and uplift rate does not match the observation that dynamic topography is nearly the same in southern and eastern Africa. The predicted values are much more confined to eastern Africa and appear to be inconsistent with the broad African Superswell [e.g., *Nyblade and Robinson*, 1994]. Clearly, some additional aspect of the models must be revised to improve the fit to observed values.

[42] We can try to improve the fit by using a more realistic upper mantle viscosity structure. In order to explore the influence of variations in upper mantle viscosity, a slight change in our method was required. In our investigations we found substantial changes in the global baseline topography when lateral variations in viscosity controlled by shear velocity variations through the upper mantle were incorporated globally. This appeared to be caused by the influence of the high viscosity within subduction zones. In order to overcome this problem, while isolating the influence that different components of variable viscosity have on African uplift, we formulated regional models. With these models, flow within a full sphere was solved but with density anomalies and lateral variations in viscosity confined to the African region (latitude: 50°N to 50°S, longitude: 30°W to 70°E). Global and regional models with solely radial variations in viscosity give similar values for dynamic topography and uplift within the African region (compare case 12 with case 4, Table 2).

6.4. Continental Root

[43] A high-viscosity lid, which is thickest beneath continents, can strongly influence topography and uplift rate. In the regional
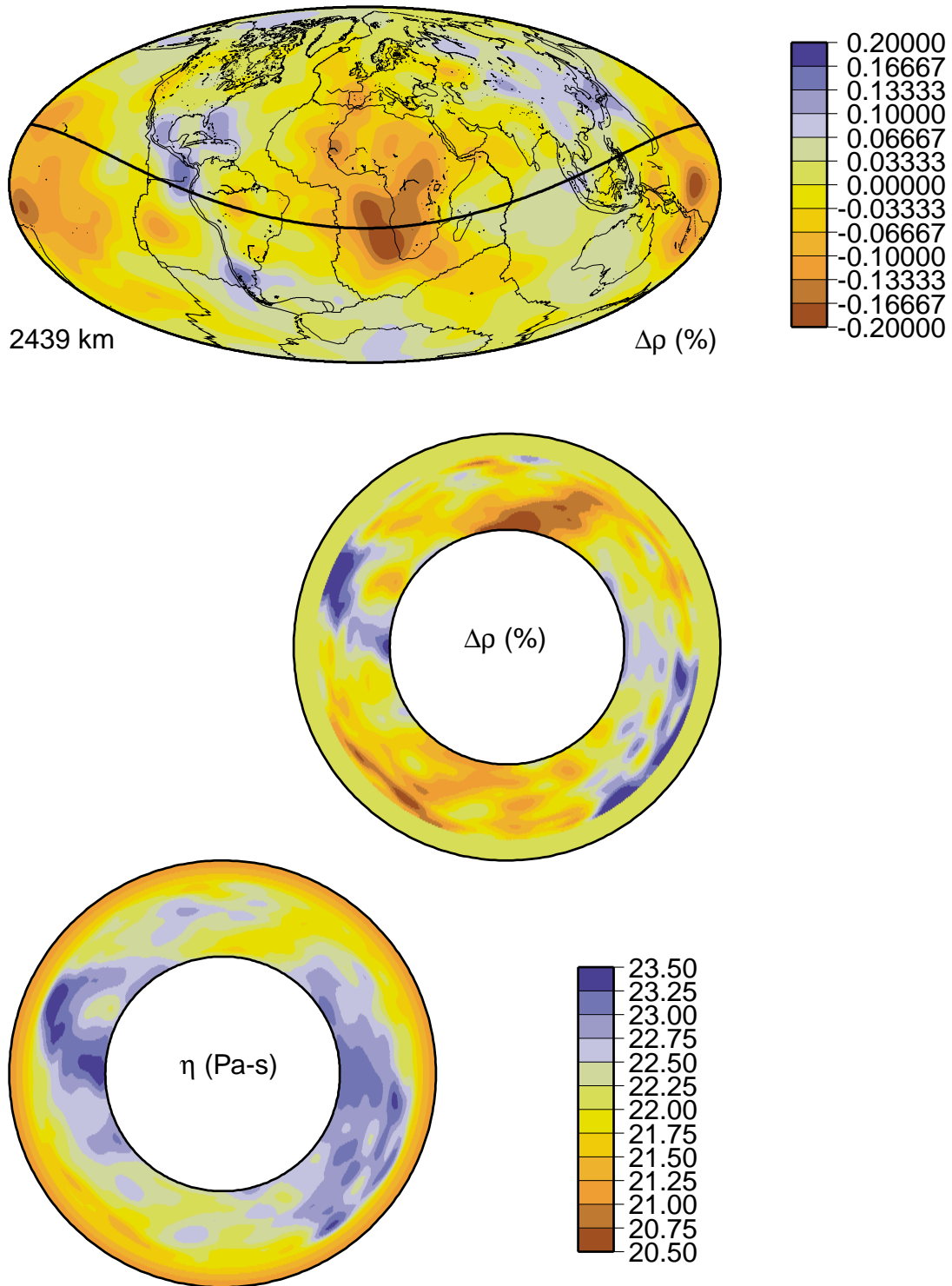
Figure 11. Density and viscosity cross section along a great circle for case 10 with temperature-dependent viscosity. The density at a depth of 2439 km is shown at the top.

models we systematically varied lid thickness and temperature-dependent viscosity. When temperature-dependent viscosity is included (case 13) the uplift rate more than doubles with only a modest increase in dynamic topography (compared to case 12), in accord with the results of the global models. If only a lid (with a thickness of 150 km and a viscosity of 10^{23} Pa s) is present without temperature-dependent viscosity (case 14), dynamic topography and uplift rate only increase by modest amounts.

[44] We can increase the coupling of the surface with the lower mantle African anomaly if lateral variations in viscosity through the upper mantle are allowed. So far, lateral variations in viscosity within the upper mantle have not been incorporated into our mantle models. However, as seen in the tomography model, high shear wave velocity anomalies extend through the upper mantle into the transition zone beneath southern Africa (Figures 1B and 1D), and these can be mapped into viscosity variations. While continuing to set density anomalies above 660 km to zero, we perform calculations in which seismic velocities are allowed to influence viscosity through (7) and (8). In the case when lateral variations in viscosity extend up to 200 km, while the lid extends down to 150 km (case 15), we obtain results that are on average close to case 13. Uplift rate in southern Africa increases with the stronger coupling. This is particularly evident when the high-viscosity lid and the lateral variations in upper mantle viscosity overlap (cases 16 and 17). In map view a second region of high uplift rates extends into southern Africa (Figures 6E and 6F). The reason for the increased coupling can be seen in the driving density and viscosity from a cross section through the African region down to the core-mantle boundary (Figure 12). The anomaly directly beneath southern Africa is located at depths larger than 2000 km, and it

does not excite significant deformation at the Earth's surface. However, from $15°$ to $20°$ along profile $a-a'$ in Figure 12, we can see that the deep mantle low-density structure is overlain by high-viscosity lower mantle. This high-viscosity region extends through the upper mantle and connects to the High-viscosity lid beneath southern Africa. Although the average value of dynamic topography and uplift rate within the African region does not dramatically increase from case 14 to 16 with the presence of upper mantle viscosity variations (Table 2), the peak values within southern Africa do. Figures 6E and 6F show that topography and uplift rate now approach values, ≈ 400m and 4 m/Myr, compatible with geologic values.

6.5. Depth-Dependent Density Scaling

[45] As another approach to improving the fit between calculated dynamic topography and observed residual topography, as well as obtaining appreciable values of uplift rate in southern Africa, $\partial \rho / \partial v_s$ was made depth-dependent in some models. Inspection of the tomography results (Figure 1) shows that the correlation of low shear velocity anomalies with the topography of southern Africa peaks at ≈ 2000-km depth. We explore a number of models in which this region as well as the lowermost mantle are accentuated (Figure 13). First, using scaling S1 in which $\partial \rho / \partial v_s$ increases by a factor of 4 within the lowermost ~ 1000 km of the mantle leads to large increases in topography and uplift rate within the African region. The uplift rate field in particular becomes broader than evident in the model with a constant $\partial \rho / \partial v_s$ scaling. This model does not resolve the problem of nearly uniform high topography and uplift rate between eastern and southern Africa. The region between 1500- and 2500-km depth is accentuated in two cases associated with scaling S2 and S3. In case 20
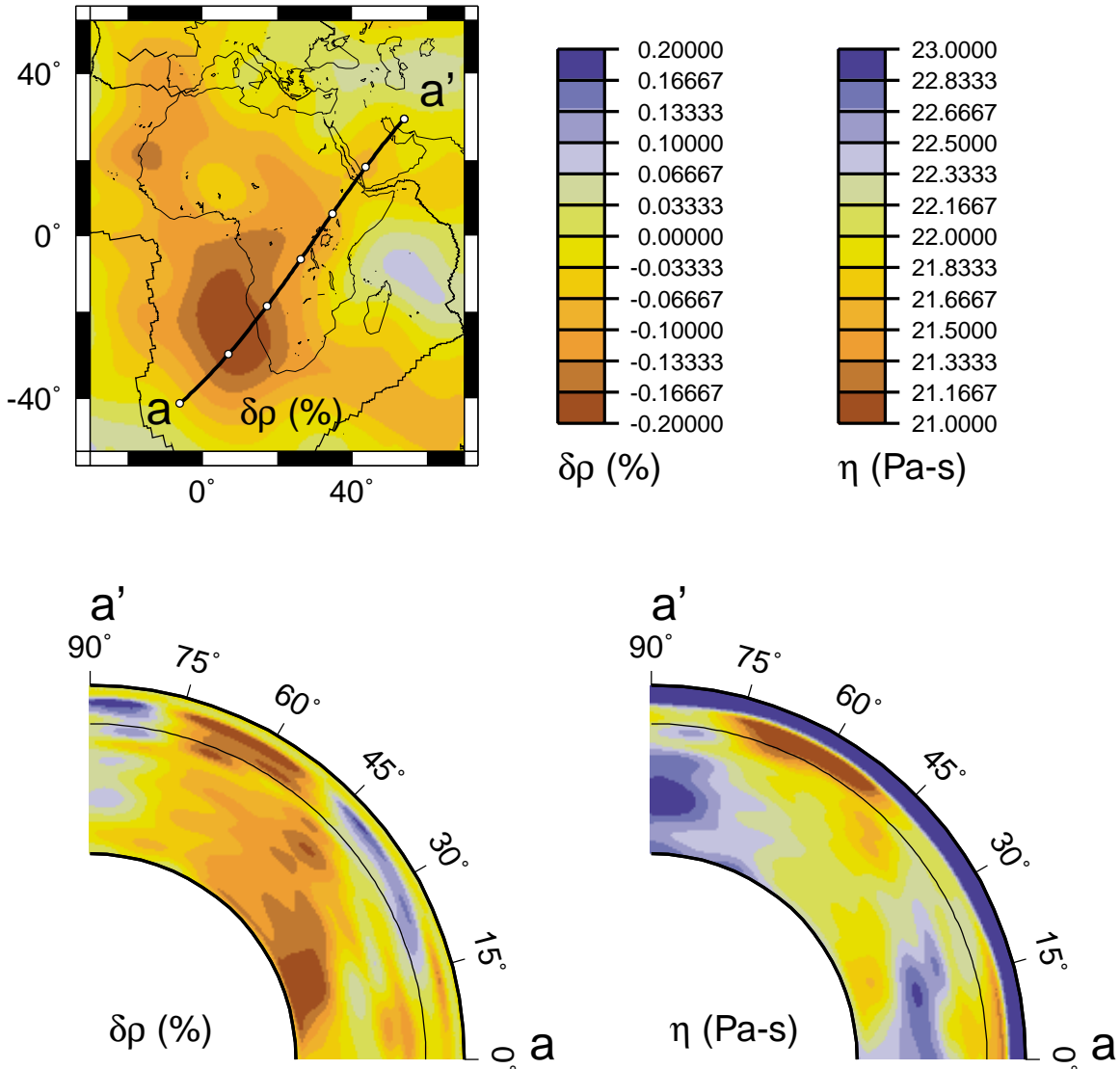
Figure 12. Cross sections through the density field (shown at 279 km above the CMB) and viscosity are shown for case 16. Note that variations in density above a depth of 660 km (denoted by thin black line) do not drive the flow: They are only shown to demonstrate the controls on the viscosity fields shown in the panel on the right.

$(\partial\rho/\partial v_s = 400$ kg m^{-3}/km s$^{-1})$, a more uniform distribution of high topography is found between eastern and southern Africa. Finally, when a high-viscosity lid and lateral variations in viscosity are incorporated then appreciable high topographies are found in southern and eastern Africa and high uplift rates through the African Superswell. For

completeness, we also consider an additional model, S4 (Figure 13D), in which the sign of $\partial\rho/\partial v_s$ reverses within the lowermost ~500 km of the mantle in a maner akin to the results of *Ishii and Tromp* [1999]. This high-density anomaly immediately below the low-density mid-lower mantle decreases the dynamic topography and halves the uplift rate.
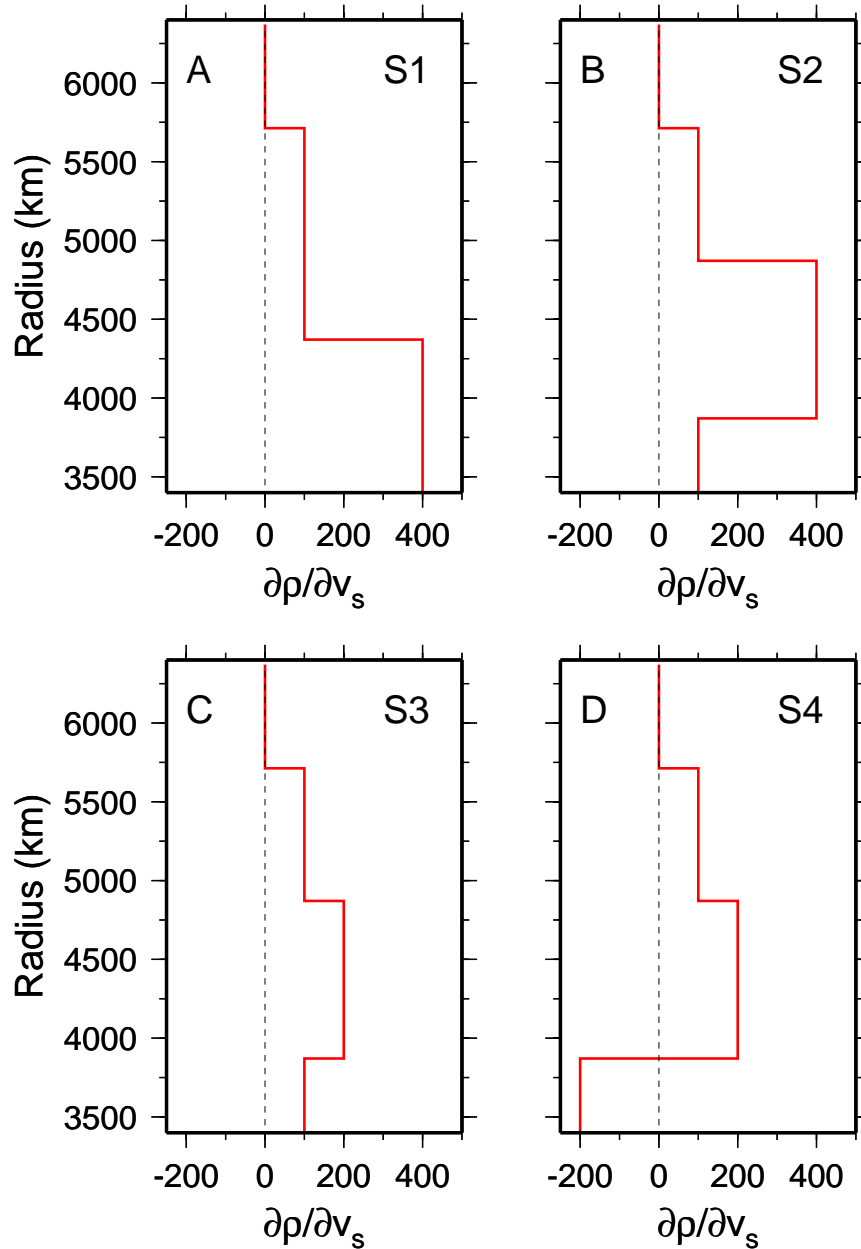
Figure 13. Four depth-dependent $\partial\rho/\partial v_s$ scalings (units of this scaling are kg m^{-3}/km s^{-1}).

Interestingly, two maxima now appear in the uplift rate fields (Figures 6G and 6H) (one within eastern Africa and the second within southern Africa). In this case we actually obtain a difference in the position of the maximum of dynamic topography (which is in eastern Africa) and uplift rate (which is in southern Africa).
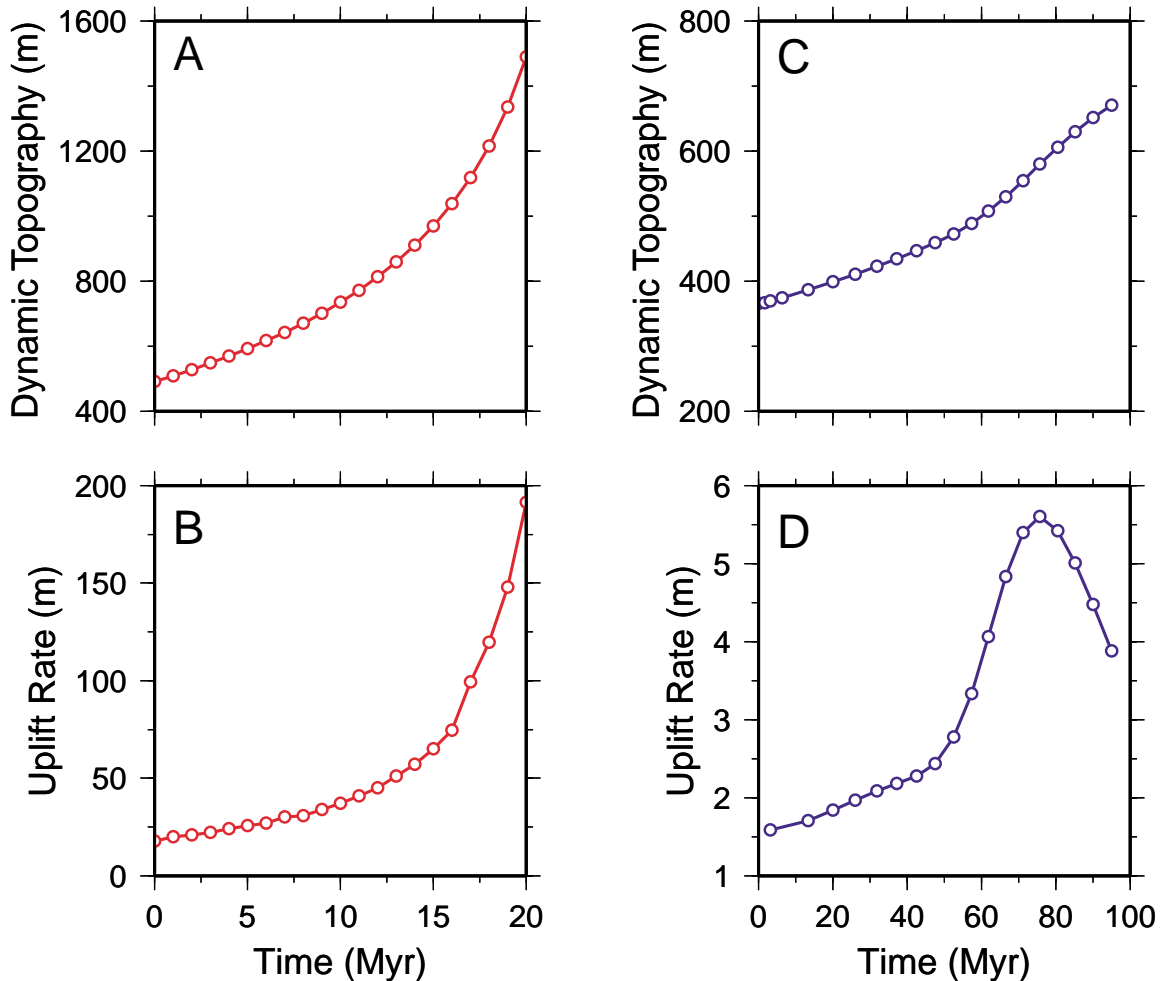
Figure 14. (A) Dynamic topography as a function of time for an isolated plume characterized by a peak density anomaly of −2% (mean density anomaly of −1%) rising in a mantle with a radial viscosity profile given by the dotted line in Figure 4A (i.e., viscosity increasing by 50 from the surface to the CMB). (B) Uplift rate for the same model as in Figure 14A. (C, D) Topography and uplift rate for a long time integration of case 10 (initial state shown in Figure 11).

7. The History of Uplift

[46] Because none of the dynamic models we have studied is in a steady state, neither dynamic topography nor uplift rate are constant in time. Because we have attempted to find models consistent with present-day dynamic topography and uplift rate, what will such models predict and will they continue to be consistent with observations if they are integrated forward

in time? We address such questions with our axisymmetric flow model and a spherical flow model constrained from present-day seismic tomography.

[47] Consider the axisymmetric model plume with a peak density anomaly of −2% rising in a mantle characterized by a viscosity that increases by a factor of 50 from the surface to the CMB. From Figure 5A the initial

dynamic topography and uplift rate associated with this nearly spherical plume are 490 m and 17 m/Myr, consistent with the bounds on present-day topography and average uplift rate. The evolution of the dynamic topography for this specific case is tracked for 20 Myr (Figure 14A). In just 15 Myr the model plume has risen sufficiently so that dynamic topography has doubled (to ~1000 m) and uplift rate has nearly quadrupled (to ~65 m/Myr). This trend continues to escalate so that dynamic topography has increased to geologically unreasonable values.

[48] The longer-term implications of a model with its initial condition derived from seismic tomography were also explored. Case 10, in which $\partial\rho/\partial v_s$=100 kg m^{-3}/km s^{-1} and a temperature-dependent viscosity, was integrated forward in time. The initial density and viscosity through the upper mantle was set to zero, but the density field was allowed to advect into the upper mantle as the model evolved. The dynamic topography monotonically increases even as the uplift rate dramatically increases for a short period (Figures 14C and 14D). Eventually, the dynamic topography levels off at ~700 m as the uplift rate starts to decrease after the low-density, low-viscosity upwelling impinges the surface and moves horizontally outward. Because the density variations exist through the whole lower mantle, the change as a function of time is less dramatic than was the case for the isolated plume at the base of the mantle (Figures 14A and 14B).

8. Discussion and Conclusions

[49] We have attempted to find dynamic models of the Earth's mantle consistent with the present-day elevated topography of southern Africa (≈300–600 m), an average uplift rate (≈5–30 m/Myr), and a buoyancy force in which the geometry was obtained from a new seismic shear velocity model of the mantle. The primary free parameters were the density of the anomaly driving the flow and mantle viscosity. Although we are unable to find a perfect fit to all constraints simultaneously, the best fitting models have the following characteristics. Within the mid-lower mantle, between ~1500 and ~2500 km depth, the anomalous density is ~−0.2% or ~10 kg m^{-3} and the viscosity is rather low, 10^{21} to 10^{22} Pa s. In order to have southern Africa attain about the same dynamic topography and uplift rate as predicted for east Africa, the variable viscosity and a complex shear velocity to density scaling appear to be needed. Our conclusion that the lower half of the lower mantle sustains the high elevations of southern Africa is similar to the conclusion of *Lithgow-Bertelloni and Silver* [1998], although we used a smaller $\partial\rho/\partial v_s$, presumably because of the smaller midmantle shear velocity anomalies in the *Grand et al.* [1997] tomographic model compared with S20RTS.

[50] Qualitatively, small density differences are needed to reduce dynamic topography to reasonable levels (e.g., less than about 500 m) while rather low viscosities, at least compared to viscosities that are normally thought to occur within the lower mantle, appear to be needed to bring uplift rates up to acceptable values in the presence of small densities. Invoking a temperature-dependent viscosity, that is, assuming the low shear velocities observed beneath Africa are due to higher temperatures, provides a self-consistent means by which to obtain relatively small lower mantle viscosities beneath southern Africa. Temperature-dependent viscosity also increases the viscosity beneath the major subduction zones of the circum Pacific giving rise to radial gradients inferred from studies of the geoid over subduction zones [e.g. *Hager*, 1984].

[51] As an alternative model, we explored the possibility raised by *Nyblade and Robinson* [1994] and *Burke* [1996] that southern Africa

is raised upward by a high-temperature, low-density anomaly directly beneath the lithosphere. Tomographic inversions, including both the model S20RTS described here as well as a regional model of the African upper mantle discussed by *Ritsema and van Heijst* [1999], show no evidence for low shear wave speeds in the upper mantle beneath the southern portion of the continent. With a flattened plume directly beneath the lithosphere (400 km thick and with $\delta v_s \sim -0.3\%$ to $\sim -0.6\%$) a rather moderate anomaly can explain the high topography but not the uplift rate, which we predict to be insignificant (Figures 6A and 6B). Models fitting the excess topography have a linear trade-off between thickness and density (seismic velocity) so that a 200 km, $\delta v_s \sim -1\%$ anomaly would also be possible. Such velocities are neither consistent with S20RTS nor with studies using regional surface waves [*Cichowicz and Green*, 1992] or regional body wave data [*Zhao et al.*, 1999]. Our shallow dynamic model is limited in that the buoyant mantle could have ascended earlier in the Cenozoic and moved laterally beneath the lithosphere (as suggested by *Artyushkov and Hofmann* [1998]). However, this seems to be incompatible with continuing uplift and possibly even increasing rates of uplift today [*Partridge and Maud*, 1987]. It must be emphasized that there is no extensive volcanism within southern Africa today [*Burke*, 1996], and this appears to rule out a thermal anomaly directly beneath or within the lithosphere. Therefore the absence of present-day volcanism is fully compatible with the high shear velocities within the upper mantle beneath southern Africa.

[52] The most significant discrepancies between simple models and observations involve the geometry of topography and uplift rate. The magnitude of both residual topography (Figure 3) and epeirogenic uplift appears to be comparable in southern and eastern Africa. However, the morphology of the African mantle anomaly

(see also *Ritsema et al.* [1999]) is tilted from the vertical such that the anomaly is beneath the south Atlantic/southern Africa at the core mantle boundary (CMB) and beneath the Afar region within the upper mantle (Figure 1B). With the shape of this internal load the highest topographies and uplift rates occur in east Africa (Figures 6C and 6D) above mantle anomalies between $\sim$660- and $\sim$1000-km depths within the lower viscosity portions of the mantle (Figure 4).

[53] Southern Africa can be elevated more effectively by lower mantle buoyancy sources if a thick continental root viscously couples the surface to the lower mantle. Fast shear velocities are particularly pronounced below southern African to a depth of 200–300 km (Figures 1B–1D) [*Ritsema and van Heijst*, 1999]. *Pollack* [1986] has argued that continental roots are probably strong (that is, have a high effective viscosity); consequently, thick continental roots could effectively cut across the normally low viscosity upper mantle and increase the coupling between the lower mantle and surface. We have demonstrated, using models incorporating variable viscosity within the upper mantle, that the uplift of southern Africa can increase owing to this mechanism (Figures 6E and 6F).

[54] We have found that the most effective means to increase the predicted uplift of southern Africa to values comparable to east Africa is to incorporate a $\partial \rho / \partial v_s$ scaling that is depth dependent. Although other scalings presumably could be found to satisfy the surface constraints, we have chosen to adopt a set of simple scalings in which the region between 1500- and 2500-km depth is accentuated (Figures 13B–13D). It is possible in this case to increase both dynamic topography and uplift rates in southern Africa to values comparable to those in east Africa (Figures 6G–6H).

[55] Our results are not particularly sensitive to $\partial\rho/\partial v_s$ at the very base of the lower mantle. The geological observations do not force us to use a $\partial\rho/\partial v_s < 0$ within 500 km of the CMB, but we are motivated to consider this possibility by the normal mode inversion by *Ishii and Tromp* [1999]. Although we can tolerate models in which the lowermost part of the mantle is denser beneath southern Africa, it is essential that the region above this (e.g., the mid-lower mantle) be lower density. We thus find that the results of *Ishii and Tromp* [1999] are not incompatible with dynamic uplift of southern Africa by a positively buoyant lower mantle source. This density model of the mantle (e.g., a high-density anomaly surrounded by a low-density halo) could be particularly diagnostic of mantle dynamics. Indeed, it is akin to dynamic models of mantle convection in which high-density mantle dregs accumulate to the base of the hot upwelling mantle [*Gurnis*, 1986]. Indeed, independent of the means by which such a dense structure is formed, either as a relic of an ancient preexisting layer [*Davies and Gurnis*, 1986; *Sidorin and Gurnis*, 1998; *Tackley*, 1998], by chemical reaction or infiltration from the core [*Hansen and Yuen*, 1988], or by continuous segregation of oceanic crust from subducted slabs [*Gurnis*, 1986; *Christensen and Hofmann*, 1994] within less than ~100 Myr, the dense material is swept away from downwellings to the base and central parts of upwellings.

[56] *Partridge and Maud* [1987] have estimated extreme values for Pliocene uplift amounting to 900 m in Natal. We estimate the uplift rates would range from ~30 to ~80 m/Myr. We did not find the evidence on which this estimate is based (difficult to correlate Post African surfaces) to be compelling. Nevertheless, the question arises as to whether a rising plume can account for this uplift history. When the anomaly is located at great depths in the mantle, topography and uplift rates will drama-

tically increase as the plume ascends and give topographies which are geologically unreasonable [e.g., *Gurnis*, 1990]. However, when our prefered model is integrated forward in time, topography will only moderately increase above values that we predict for the present-day (Figures 14C and 14D). If the inference of Pliocene uplift inferred by *Partridge and Maud* [1987] is robust, we conclude that it could not have been the result of a deep mantle thermal anomaly.

[57] Finally, the long time integrations (Figure 14) illustrate another limitation of our comparison of model results to geology: Topography and uplift rate are unlikely to be steady in time over a ~30-Myr period, the approximate time interval over which uplift rates have been averaged. A more realistic comparison between model and observation would use Present-day topography and tomography as constraints on an evolutionary model that is compared to observed uplift as a function of time. In such an evolutionary model we could either guess mantle structure at some point in the past or estimate it by integrating (2)–(4) backward in time.

[58] In summary, southern Africa is geologically a unique plateau with about 450 m of excess elevation with neither extensive recent volcanism nor present-day orogenic activity. The plateau appears to have developed since the Mesozoic at rates between 5 and 30 m/Myr. We believe that this plateau is unique because it overlies the strongest and largest low shear velocity anomaly in the lower mantle. If the mid-lower mantle is moderately low density (~−0.2%) with a viscosity of ~10^{21} to ~10^{22} Pa s, then the dynamics are consistent with the surface constraints. The uplift of southern Africa is augmented by a thick, strong cratonic keel that cuts across the normally weak upper mantle. The basal, central region of this low-density, presumably high-

temperature, mantle anomaly could be characterized by an anomalously high density as predicted by dynamic models of thermochemical convection.

Acknowledgments

References

Adams, J., MUDPACK: Multigrid fortran software for the efficient solution of linear elliptic partial differential equations, *Appl. Math. Comput.*, *34*, 113–146, 1989.

Artyushkov, E. V., and A. W. Hofmann, Neotectonic crustal uplift on the continents and its possible mechanisms. The case of souhern Africa, *Surv. Geophys.*, *19*, 369–415, 1998.

Bolton, H., Long period travel times and the structure of the mantle, Ph.D. thesis, Univ. of Calif., San Diego, 1996.

Brooks, A. N., A Petrov-Galerkin finite element formulation for convection dominated flows, Ph.D. thesis, Calif. Inst. of Technol., Pasadena, 1981.

Brown, R. W., K. Gallagher, A. J. W. Gleadow, and M. A. Summerfield, Morphotectonic evolution of the South Atlantic margins of Africa and South America, *Geomorphology and Global Tectonics*, edited by M. A. Summerfield, pp. 255–280, John Wiley, New York, 2000.

Burke, K., The African Plate, *S. Afr. J. Geol.*, *99*, 341–409, 1996.

Chase, C. G., Subduction, the geoid, and lower mantle convection, *Nature*, *282*, 464–468, 1979.

Christensen, U. R., and A. W. Hofmann, Segregation of subducted oceanic crust in the convecting mantle, *J. Geophys. Res.*, *99*, 19,867–19,884, 1994.

Cichowicz, A., and R. W. E. Green, Tomographic study of upper mantle structure of the South African continent, using waveform inversion, *Phys. Earth Planet. Int.*, *72*, 276–285, 1992.

Cogley, J. G., Hypsometry of the continents, *Z. Geomorphol.*, *53*, 1–48, 1985.

Crough, S. T., Hotspot swells, *Ann. Rev. Earth Planet. Sci.*, *11*, 165–193, 1983.

Davies, G. F., and M. Gurnis, Interaction of mantle dregs with convection: Lateral heterogeneity at the core-mantle boundary, *Geophys. Res. Lett.*, *13*, 1517–1520, 1986.

Davies, G. F., and F. Pribac, Mesozoic seafloor subsidence and the Darwin Rise, past and present, in *The Mesozic Pacific: Geology, Tectonics, and Volcanism, Geophys. Monogr. Ser.*, vol. 77, edited by M. S. Pringle et al., pp. 39–52, AGU, Washington, D. C., 1993.

Dingle, R. V., Continental margin Subsidence: A comparison between the east and west coasts of Africa, in *Dynamics of Passive Margins, Geodyn. Ser.*, vol. 6, edited by R. A. Scrutton, pp. 59–71, AGU, Washington, D. C., 1982.

Dziewonski, A. M., Mapping the lower mantle: Determination of lateral heterogenity in *P* velocity up to degree and order 6, *J. Geophys. Res.*, *89*, 5929–5952, 1984.

Dziewonski, A. M., and J. H. Woodhouse, Global images of the Earth's interior, *Science*, *236*, 37–48, 1987.

Forte, A. M., J. X. Mitrovica, and R. L. Woodward, Seismic-geodynamic determination of the origin of the excess ellipticity of the core-mantle boundary, *Geophys. Res. Lett.*, *22*, 1013–1016, 1995.

Gallagher, K., and R. Brown, Denudation and uplift at passive margins: The record on the Atlantic margin of southern Africa, *Philos. Trans. R. Soc. London, Ser. A*, *367*, 835–859, 1999.

Grand, S. P., R. D. van der Hilst, and S. Widiyantoro, Global seismic tomography: A snapshot of convection in the Earth, *GSA Today*, *7*(4), 1–7, 1997.

Griffiths, R. W., M. Gurnis, and G. Eitelberg, Holographic measurements of surface topography in laboratory models of mantle hotspots, *Geophys. J.*, *96*, 477–495, 1989.

Gurnis, M., The effects of chemical density differences on convective mixing in the Earth's mantle, *J. Geophys. Res.*, *91*, 11,407–11,419, 1986.

Gurnis, M., Bounds on global dynamic topography from Phanerozoic flooding of continental platforms, *Nature*, *344*, 754–756, 1990.

Hager, B. H., Subducted slabs and the Geoid: Constraints on mantle rheology and flow, *J. Geophys. Res.*, *89*, 6003–6015, 1984.

Hager, B. H., R. W. Clayton, M. A. Richards, R. P. Comer, and A. M. Dziewonski, Lower mantle heterogeneity, dynamic topography and the geoid, *Nature*, *313*, 541–545, 1985.

Hallam, A., *Phanerozoic Sea-Level Changes*, 266 pp., Columbia Univ. Press, New York, 1992.

Hansen, U., and D. A. Yuen, Numerical simulations of

thermal-chemical instabilities at the core-mantle boundary, *Nature*, *334*, 237–240, 1988.

Harrison, C. G. A., K. J. Miskell, G. W. Brass, E. S. Saltzman, and J. L. Sloan, Continental hypsography, *Tectonics*, *2*, 357–377, 1983.

Ishii, M., and J. Tromp, Normal-mode and free-air gravity constraints on lateral variations in velocity and density of Earth's mantle, *Science*, *285*, 1231–1236, 1999.

Jordan, T. H., The continental tectosphere, *Rev. Geophys.*, *13*, 1–12, 1975.

Kennett, B. L. N., S. Widiyantoro, and R. D. van der Hilst, Joint seismic tomography for bulk sound and shear wave speed in the Earth's mantle, *J. Geophys. Res.*, *103*, 12,469–12,493, 1998.

King, L. C., *The Morphology of the Earth*, 699 pp., Oliver and Boyd, Edinburgh, 1962.

Kuo, C., and B. Romanowicz, Density and seismic selocity variations in the mantle determined from normal mode spectrum (abstract), *Eos Trans. AGU*, *80*(17), Spring Meet. Suppl., S14, 1999.

Laske, G., and G. A. Masters, Global digital map of sediment thickness (abstract), *Eos Trans. AGU*, *78*(46), Fall Meet. Suppl., F483, 1997.

Li, X. D., and B. Romanowicz, Global mantle shear velocity model developed using nonlinear asymptotic coupling theory, *J. Geophys. Res.*, *101*, 22,245–22,272, 1996.

Lithgow-Bertelloni, C., and M. Gurnis, Cenozoic subsidence and uplift of continents from time-varying dynamic topography, *Geology*, *25*, 735–738, 1997.

Lithgow-Bertelloni, C., and P. G. Silver, Dynamic topography, plate driving forces and the African superswell, *Nature*, *395*, 269–272, 1998.

Marsh, J. G., et al., The GEM-T2 gravitational model, *J. Geophys. Res.*, *95*, 22,043–22,071, 1990.

Marty, J. C., and A. Cazenave, Regional variations in subsidence rate of oceanic plates: A global analysis, *Earth Planet. Sci. Lett.*, *94*, 301–315, 1989.

Masters, T. G., S. Johnson, G. Laske, and H. Bolton, A shear-velocity model of the mantle, *Philos. Trans. R. Soc. London, Ser. A*, *354*, 1385–1411, 1996.

Masters, G., H. Bolton, and G. Laske, Joint seismic tomography for P and S velocities: How pervasive are chemical anomalies in the mantle? (abstract), *Eos Trans. AGU*, *80*(17), Spring Meet. Suppl., S14, 1999.

Maud, R. R., T. C. Partridge, and W. G. Siesser, An early Tertiary marine deposit at Pato's Kop, Ciskei, *S. Afr. J. Geol.*, *90*, 231–238, 1987.

McKenzie, D. P., J. M. Roberts, and N. O. Weiss, Convection in the Earth's mantle: Towards a numerical simulation, *J. Fluid Mech.*, *62*, 465–538, 1974.

McNutt, M. K., and K. M. Fischer, The South Pacific Superswell, in *Seamounts, Islands and Atolls, Geophys.*

Monogr. Ser., edited by B. T. Tsurutani and H. Oya, vol. 53, pp. 25–34, AGU, Washington, D. C., 1987.

Mooney, W. D., G. Laske, and G. Masters, CRUST5.1: A global crustal model at $5° \times 5°$, *J. Geophys. Res.*, *103*, 727–747, 1998.

Moresi, L., and M. Gurnis, Constraints on the lateral strength of slabs from three-dimensional dynamic flow models, *Earth Planet. Sci. Lett.*, *138*, 15–28, 1996.

Nyblade, A. A., and S. W. Robinson, The African Superswell, *Geophys. Res. Lett.*, *21*, 765–768, 1994.

Ollier, C. D., and M. E. Marker, The Great Escarpment of southern Africa, *Z. Geomorphol.*, *54*, 37–56, 1985.

Partridge, T. C., Late Neogene uplift in eastern and southern Africa and its paleoclimatic implications, in *Tectonic Uplift and Climate Change*, edited by W. F. Ruddiman, pp. 63–86, Plenum, New York, 1997.

Partridge, T. C., and R. R. Maud, Geomorphic evolution of southern Africa since the Mesozoic, *S. Afr. J. Geol.*, *90*, 179–208, 1987.

Pollack, H. N., Cratonization and thermal evolution of the mantle, *Earth Planet. Sci. Lett.*, *80*, 175–182, 1986.

Press, W. H., B. P. Flannery, S. A. Teukolsky, and W. T. Vetterling, *Numerical Recipes in C*, 2nd ed., 735 pp., Cambridge Univ. Press, New York, 1992.

Pribac, F., *Superswells due to mantle convection*, Ph.D. thesis, Aust. Natl. Univ., Canberra, 1991.

Resovsky, J. S., and M. H. Ritzwoller, A degree 8 mantle shear velocity model from normal mode observations below 3 mHz, *J. Geophys. Res.*, *104*, 993–1014, 1999.

Richter, F. M., Finite amplitude convection through a phase boundary, *Geophys. J. R. Astron. Soc.*, *35*, 265–276, 1973.

Ritsema, J., and H. J., van Heijst, New seismic model of the upper mantle beneath Africa, *Geology*, *28*, 63–66, 1999.

Ritsema, J., S. Ni, D. V. Helmberger, and H. P. Crotwell, Evidence for strong shear velocity reductions and velocity gradients in the lower mantle beneath Africa, *Geophys. Res. Lett.*, *25*, 4245–4248, 1998.

Ritsema, J., H. J. van Heijst, and J. H. Woodhouse, Complex shear wave velocity structure related to mantle upwellings beneath Africa and Iceland, *Science*, *286*, 1925–1928, 1999.

Sahagian, D., Epeirogenic motions of Africa as inferred from Cretaceous shoreline deposits, *Tectonics*, *7*, 125–138, 1988.

Schroeder, W., The empirical age-depth relation and depth anomalies in the Pacific Ocean basin, *J. Geophys. Res.*, *89*, 9873–9884, 1984.

Sidorin, I., and M. Gurnis, Geodynamically consistent seismic velocity predictions at the base of the mantle, in *The Core-Mantle Boundary Region, Geodyn. Ser.*, vol. 28, edited by M. Gurnis, M. E. Wysession, E. Knit-

tle, and B. A. Buffett, pp. 209–230, AGU, Washington, D. C., 1998.

Siesser, W. G., and R. V. Dingle, Tertiary sea-level movements around southern Africa, *J. Geol.*, *89*, 83–96, 1981.

Solheim, L. P., and W. R. Peltier, Mantle phase transitions and layered convection, *Can. J. Earth Sci.*, *30*, 881–892, 1993.

Su, W., R. L. Woodward, and A. M. Dziewonski, Degree 12 model of shear velocity heterogeneity in the mantle, *J. Geophys. Res.*, *99*, 6945–6981, 1994.

Su, W.-J., and A. M. Dziewonski, Simultaneous inversion for 3-D variations in shear and bulk velocity in the mantle, *Phys. Earth Planet. Inter.*, *100*, 135–156, 1997.

Summerfield, M. A., Plate tectonics and landscape development on the African continent, in *Tectonic Geomorphology*, edited by M. Morisawa and J. J. Hack, pp. 27–51, Allen and Unwin, Boston, Mass., 1985.

Summerfield, M. A., Tectonics, geology, and long-term landscape development, in *The Physical Geography and Africa*, edited by W. H. Adams, A. S. Goudie, and A. R. Orme, pp. 1–17, Oxford Univ. Press, New York, 1996.

Tackley, P. J., Three-dimensional simulations of mantle convection with a thermo-chemical basal boundary layer: D″?, in *The Core-Mantle Boundary Region, Geodyn. Ser.*, vol. 28, edited by M. Gurnis, M. E. Wysession, E. Knittle, and B. A. Buffett, pp. 231–253, AGU, Washington, D. C., 1998.

van der Hilst, R. D., and H. Karason, Compositional heterogeneity in the bottom 1000 kilometers of Earth's mantle: Toward a hybrid convection model, *Science*, *283*, 1885–1888, 1999.

van der Hilst, R. D., S. Widiyantoro, and E. R. Engdahl, Evidence for deep mantle circulation from global tomography, *Nature*, *386*, 578–584, 1997.

Van Heijst, H.-J., and J. H. Woodhouse, Global high-resolution phase velocity distributions of overtone and fundamental-mode surface waves determined by mode branch stripping, *Geophys. J. Int.*, *137*, 601–620, 1999.

van Heijst, H. J., J. Ritsema, and J. H. Woodhouse, Global P and S velocity structure derived from normal mode splitting, surface wave dispersion and body wave travel time data (abstract), *Eos Trans. AGU*, *80*(17), Spring Meet. Suppl., S221, 1999.

Zhao, M., C. A. Langston, A. A. Nyblade, and T. J. Owens, Upper mantle velocity structure beneath southern Africa from modeling regional seismic data, *J. Geophys. Res.*, *104*, 4783–4794, 1999.

Zhong, S., and G. F. Davies, Effects of plate and slab viscosities on the geoid, *Earth Planet. Sci. Lett.*, *170*, 487–496, 1999.

Zhong, S., and M. Gurnis, Mantle convection with plates and mobile, faulted plate margins, *Science*, *267*, 838–843, 1995.

Zhong, S., M. T. Zuber, L. N. Moresi, and M. Gurnis, The role of temperature-dependent viscosity and surface plates in spherical shell models of mantle convection, *J. Geophys. Res.*, *105*, 11,063–11,082, 2000.